Eur. Phys. J. C (2025) 85:1243
https://doi.org/10.1140/epjc/s10052-025-14996-z

THE EUROPEAN PHYSICAL JOURNAL C

Regular Article - Theoretical Physics

Quasinormal modes and greybody factors of charged symmergent black hole

Dhruba Jyoti Gogoi[1,2,a], **Beyhan Puliçe**[3,4,b], **Ali Övgün**[5,c]

[1] Department of Physics, Moran College, Moranhat, Charaideo, Assam 785670, India
[2] Research Center of Astrophysics and Cosmology, Khazar University, 41 Mehseti Street, AZ1096 Baku, Azerbaijan
[3] Faculty of Engineering and Natural Sciences, Sabancı University, 34956 Tuzla, İstanbul, Turkey
[4] Astrophysics Research Center (ARCO), The Open University of Israel, 4353701 Raanana, Israel
[5] Physics Department, Eastern Mediterranean University, North Cyprus via Mersin 10, 99628 Famagusta, Turkey

Received: 27 December 2024 / Accepted: 26 October 2025

Abstract In this paper, we investigate quasinormal modes (QNMs) and greybody factors within the framework of Symmergent gravity, an emergent gravity model with an $R + R^2$ curvature sector. Building on our previous work on static spherically-symmetric solutions [Puliçe et al. in Class Quantum Gravity 40(19):195003, 2023], we explore the effects of the key parameters, including the quadratic curvature coupling parameter $c_{\rm O}$ and the vacuum energy parameter α. For all the three perturbations considered here viz., scalar, electromagnetic and gravitational perturbations, an increase in α leads to a nearly linear rise in both oscillation frequencies and damping rates. The other parameter $c_{\rm O}$ affects the QNMs spectrum nonlinearly. Additionally, the charge Q of the black hole introduces nonlinear behavior, where higher charges amplify the black hole's electromagnetic field, resulting in increased oscillation frequencies and faster stabilization. These findings enhance our understanding of charged black hole stability and gravitational wave astrophysics. Further, the analysis of greybody factors reveals that increasing α, $c_{\rm O}$, and Q reduces the absorption of radiation, with gravitational perturbations reaching maximum absorption at slightly lower frequencies compared to electromagnetic and scalar perturbations.

1 Introduction

The Standard Model (SM) describes the strong, weak, and electromagnetic interactions as a renormalizable quantum field theory (QFT) [1], but does not account for gravity. It is unique to the flat Minkowski spacetime because of difficulties in quantizing the curved metric [2] and in transferring QFTs into curved spacetime [3,4]. In contrast to full QFTs like the SM, flat spacetime effective QFTs are expected to exhibit a closer connection to curved spacetime. This is because they are nearly classical field theories obtained by integrating out high-frequency quantum fluctuations [1,5], in the framework of both Wilsonian and one-particle-irreducible effective actions [7,8].

The SM is endowed with a physical UV cutoff (rather than a regulator) when viewed as an effective QFT [5]. This UV cutoff denoted by $\Lambda_{\wp}$, represents the scale at which a UV completion becomes relevant. As revealed by the null LHC searches [6], $\Lambda_{\wp}$ could be at any scale above a TeV. In general, in a Lorentz conserving regime, the loop momentum ℓ^{μ} lies in the interval $-\Lambda_{\wp}^2 \leq \eta_{\mu\nu}\ell^{\mu}\ell^{\nu} \leq \Lambda_{\wp}^2$, and it explicitly breaks the Poincaré (translation) symmetry. In the presence of the UV cutoff $\Lambda_{\wp}^2$, scalar mass-squareds obtain corrections proportional to $\Lambda_{\wp}^2$, and $\Lambda_{\wp}^4$ terms appear in the loop-corrected vacuum energy [5,9]. Beyond these UV sensitivities [5], gauge bosons also acquire mass-squared terms proportional to $\Lambda_{\wp}^2$, and which leads to a breaking of gauge symmetries [10,11]. In order to alleviate these unnatural UV sensitivities, the most sensible line of action would be to restore the gauge symmetries by means of the Higgs mechanism [12–14]. A hindrance to this proposal is the stark difference between the intermediate vector boson mass (Poincaré-conserving) [15] and the loop-induced gauge boson mass (Poincaré-breaking) [16]. Indeed, in the former, the vector boson mass is promoted to a scalar field, which leads to the usual Higgs mechanism [12–14]. In the latter, however, it is necessary to first find a Poincaré-breaking Higgs field. In this regard, it turns out that

[a] e-mail: moloydhruba@yahoo.in
[b] e-mail: beyhan.pulice@sabanciuniv.edu
[c] e-mail: ali.ovgun@emu.edu.tr (corresponding author)

Published online: 03 November 2025

the affine curvature, which is independent of the metric tensor and its connection, is the sought-after Higgs field in that it promotes the UV cutoff $\Lambda_{\wp}$ [17,18] and condenses to the usual metrical curvature in the minimum of the metric-affine action [19,20]. The defusion of the unnatural UV sensitivity, the restoration of gauge symmetries, the emergence of gravity, and the appearance of new particles without the necessity to couple directly to SM particles are the salient outcomes of this condensation. This whole mechanism is referred to as gauge symmetry-restoring emergent gravity or *symmergent gravity* in brief. Symmergent gravity has been constructed and applied through various stages [16,21–23], starting with the nascent idea of gauge symmetry restoration by means of curvature [24]. Some applications of Symmergent gravity can be found in [25–27,29–34].

Black holes are not isolated cosmic bodies; rather, they are dynamic entities that actively interact with their surroundings, profoundly influencing the fabric of spacetime. When a black hole is perturbed, spacetime itself ripples, creating waves that eventually die down as the system settles back to equilibrium. Understanding how these systems respond to small disturbances is a fundamental aspect of physics, providing deep insights into the nature of spacetime and gravity. The study of black hole perturbations began with pioneering work by [42], and was significantly advanced by others [43–48], leading to Chandrasekhar's seminal contributions [49,50]. At the heart of this field are quasinormal modes (QNMs), which are complex frequencies characterizing the oscillatory behavior of a black hole as it returns to a stable state after being disturbed. These modes are unique signatures that depend on the black hole's intrinsic properties, such as its mass, charge, and spin, as well as the nature of the perturbation–whether it is scalar, electromagnetic, or gravitational. The independence of QNMs from initial conditions makes them particularly valuable in probing the characteristics of black holes, offering a direct link between theoretical predictions and observable phenomena [40,41,51–103,115,116,152–155,173]. Beyond the four-dimensional Einstein-Maxwell Reissner–Nordström solution, a wide landscape of generalized charged black holes arises once additional fields or interactions are included: Einstein-Maxwell-dilaton black holes from Kaluza-Klein/string compactifications modify horizon structure and extremality [117,118]; Einstein-Born-Infeld (non-linear electrodynamics) black holes regularize the electromagnetic field and smoothly reduce to RN in the weak-field limit [119–121]; non-Abelian (Einstein-Yang-Mills) "colored" black holes provide counterexamples to simple no-hair expectations but are typically linearly unstable [122,123]; and higher-dimensional/stringy solutions include multi-charge/supersymmetric objects and charged black rings with non-spherical horizons [124,125]. Their perturbations and QNMs often show modest, theory-dependent deviations from RN while preserving linear stability in many Abelian cases; see [51] for a broad review. The study of QNMs is especially critical in the context of the ringdown phase of binary black hole mergers. During this phase, the newly formed black hole emits gravitational waves as it stabilizes, with the QNMs encoding key information about the black hole's parameters. As gravitational wave astronomy continues to grow, understanding QNMs has become increasingly important for interpreting the data from detectors like LIGO and Virgo [126,127].

Hawking radiation describes the emission of thermal radiation from black holes due to quantum effects near the event horizon. Originally, Hawking predicted that black holes emit radiation as perfect black bodies [137]. However, this idealized picture does not take into account the interaction of emitted radiation with the curved spacetime geometry surrounding the black hole. Greybody factors quantify the deviation of the emitted radiation from perfect blackbody radiation [140,162,163]. Physically, they represent frequency-dependent transmission coefficients, indicating how much radiation generated at the black hole horizon manages to escape to spatial infinity. The presence of gravitational potentials surrounding the black hole modifies and filters the emitted radiation, causing it to appear as a "greybody," meaning it emits radiation at intensities lower than a perfect blackbody at certain frequencies. Crucially, QNMs and greybody factors are deeply interconnected: the peaks in the greybody spectrum are often closely related to QNM frequencies, since QNMs represent resonances of the black hole spacetime. In other words, the greybody factors reflect how effectively certain QNM frequencies propagate away from the black hole, linking the black hole's emission properties directly to its intrinsic vibration modes.

Complementing the study of QNMs is the analysis of the greybody factor, which describes the modification of the spectrum of radiation as it escapes the black hole's gravitational well. The greybody factor plays a crucial role in understanding the energy distribution of radiation emitted by black holes, influencing the signals detected by gravitational wave observatories. Together, QNMs and the greybody factor provide a comprehensive picture of black hole dynamics and their interactions with the surrounding environment.

In light of this, our study focuses on computing QNMs and greybody factors for charged symmergent black holes (CSBHs). By examining these scenarios, we aim to uncover novel insights into the behavior of black holes in complex electromagnetic environments, contributing to a deeper understanding of these enigmatic objects in the universe.

Our work is organized as follows: after the introduction, we briefly review the CSBHs in Sect. 2. In Sect. 3, we investigate massless scalar and massless vector perturbations around the black hole. In Sect. 4, we study greybody factor using the WKB approach and rigorous bounds. Finally, we summarize and conclude our paper in Sect. 5.

2 Brief review of charged symmergent black holes

Symmergent gravity is a specific form of emergent gravity that incorporates both R and R^2 curvature terms along with a non-zero cosmological constant. As a specialized case within the broader class of $f(R)$ gravity theories, it was first introduced in [23,24], with further refinements and enhancements presented in [22]. This model has been applied across various contexts [27,30,31], while recent field-theoretic and string-theoretic developments have been detailed in [21]. In fact, symmergent gravity is defined by the action

$$S[g] = \int d^4x\sqrt{-g}\left\{\frac{R}{16\pi G} - \frac{c_{\rm O}}{16}R^2 - V_{\rm O} + \mathcal{L}_{matter}\right\}, \tag{1}$$

in which R is the Ricci curvature scalar and $\mathcal{L}_{matter}$ represents the Lagrangian for both standard model matter fields (quarks, leptons, gauge bosons, and the Higgs) and additional fields required to generate the inverse Newton's constant at one loop in the flat spacetime effective action. The relationship for the inverse of Newton's constant is given by

$$\frac{1}{G} = \frac{{\rm str}\left[\mathcal{M}^2\right]}{8\pi}, \tag{2}$$

which is set by the mass-squared matrix $\mathcal{M}^2$ of the entirety of matter fields such that its supertrace ${\rm str}[\mathcal{M}^2] = \sum_i(-1)^{2s_i+1}(2s_i+1){\rm tr}[\mathcal{M}^2]_{s_i}$ runs over all fields ψ_i with spin s_i. At the one-loop level, the quadratic curvature coefficient in Eq. (1) is given by the number difference between the total bosonic degrees of freedom n_B and the fermionic degrees of freedom n_F in the underlying QFT [16], namely

$$c_{\rm O} = \frac{n_{\rm B} - n_{\rm F}}{128\pi^2}. \tag{3}$$

Similarly, again at the one-loop level, the vacuum energy in Eq. (1) is given by

$$V_{\rm O} = \frac{{\rm str}\left[\mathcal{M}^4\right]}{64\pi^2}. \tag{4}$$

The loop-induced parameters $n_{\rm B}$ and $n_{\rm F}$ play a crucial role in determining key aspects of the Symmergent gravity. These degrees of freedom are not limited to the known particles of the standard model; they also encompass entirely new particles, both massive and massless, that may not interact with the SM particles non-gravitationally. This broader inclusion of particle species highlights the flexibility of Symmergent gravity, allowing it to incorporate new physics beyond the SM without requiring couplings to the known particles. Consequently, the contributions from these additional particles affect the gravitational sector primarily through their impact on loop corrections, influencing the effective gravitational dynamics.

In the context of general $n_{\rm B}$ and $n_{\rm F}$, the Symmergent gravity action (1) may be expressed in the $f(R)$ gravity form as shown below [27]:

$$S[g] = \frac{1}{16\pi G}\int d^4x\sqrt{-g}\left(f(R) - 2\Lambda - \frac{1}{2}\hat{F}_{\mu\nu}\hat{F}^{\mu\nu}\right) \tag{5}$$

where $f(R) = R + \beta R^2$ with the quadratic curvature coefficient $\beta = -\pi G c_{\rm O}$ and the cosmological constant $\Lambda = 8\pi G V_{\rm O}$. A detailed analysis of the vacuum energy $V_{\rm O}$ starting from its definition in Eq. (4), will be presented in the subsequent part of the paper.

In this paper, we focus solely on the electromagnetic field from the matter sector in the action (5). The electromagnetic field tensor is given by

$$\hat{F}_{\mu\nu} = \partial_\mu\hat{A}_\nu - \partial_\nu\hat{A}_\mu \tag{6}$$

where the dimensionless electromagnetic potential is defined as $\hat{A}_\mu = A_\mu/\sqrt{8\pi G}$.

In this section, we derive the charged black hole solution for the combined Symmergent gravity and Maxwell system from the action in (5). The gravitational field equations are expressed as follows,

$$E_{\mu\nu} \equiv R_{\mu\nu}F(R) - \frac{1}{2}g_{\mu\nu}f(R) + g_{\mu\nu}\Lambda + (g_{\mu\nu}\Box - \nabla_\mu\nabla_\nu)F(R) - \hat{T}_{\mu\nu} = 0 \tag{7}$$

and are coupled with the Maxwell field equations:

$$\partial_\mu(\sqrt{-g}\hat{F}^{\mu\nu}) = 0 \tag{8}$$

where $F(R) \equiv df(R)/dR$ and $\hat{T}_{\mu\nu}$, the energy–momentum tensor of the dimensionless Maxwell field in (7), is given by:

$$\hat{T}_{\mu\nu} = g^{\alpha\beta}\hat{F}_{\alpha\mu}\hat{F}_{\beta\nu} - \frac{1}{4}g^{\gamma\alpha}g^{\rho\beta}\hat{F}_{\alpha\beta}\hat{F}_{\gamma\rho}. \tag{9}$$

We now seek a static, spherically symmetric solution for the combined Symmergent gravity and Maxwell system. For this, we propose the following metric:

$$ds^2 = -h(r)dt^2 + \frac{1}{h(r)}dr^2 + r^2(d\theta^2 + \sin^2\theta d\phi^2), \tag{10}$$

where $h(r)$ is the single metric potential. The corresponding electromagnetic scalar potential is $\hat{A}_0 = \hat{q}(r)$, with the vector potential vanishing ($\hat{A}_i = 0$, for $i = 1,2,3$). The electrostatic potential is given by: $\hat{q}(r) = \frac{Q}{r}$ where a homogeneous term has been discarded, ensuring the scalar potential follows a pure Coulomb form. For a QFT characterized by a scale M_0 but lacking detailed knowledge of the mass spectrum, realistic scenarios can be modeled by introducing the parametrization:

$$V_{\rm O} = \frac{1-\alpha}{(8\pi G)^2 c_{\rm O}}, \tag{11}$$

where the parameter α reflects deviations in the boson and fermion masses from the characteristic scale M_0. In general, $\alpha > 1$ ($\alpha < 1$) indicates fermion (boson) dominance in terms of the trace of (masses)^4, with $\alpha > 1$ corresponding to an AdS spacetime and $\alpha < 1$ corresponding to a dS spacetime.

With the vacuum energy given by Eq. (11), the metric potential $h(r)$ takes the form [27]:

$$h(r) = 1 - \frac{2MG}{r} + \frac{Q^2}{2\alpha r^2} - \frac{(1-\alpha)}{24\pi G c_{\rm O}} r^2. \tag{12}$$

It results in the standard Reissner–Nordström-AdS/dS black hole when $\hat{Q}^2 = \frac{Q^2}{2\alpha}$ and $\hat{\Lambda} = \frac{(1-\alpha)}{8\pi G c_{\rm O}}$. The metric (10) with the potential (12) is called as CSBH [27].

The predictions of the Einstein field equations have been tested extensively in a broad range of observationally accessible scenarios [28], including but not limited to inflationary evolution [29], the formation of neutron stars and black holes [26,27,30–35], and the emission of gravitational waves [36,37]. Given the increase in the number and variety of astrophysical observations of ultracompact objects (inlcuding recent EHT [38] and JWST [39] observations), black holes manifest themselves as viable testbeds. This motivates our study of black hole spacetimes depending on the parameters $c_{\rm O}$ and α.

The allowed domain of the Symmergent parameters is constrained by both theoretical consistency and observational requirements. In our previous work on charged symmergent black holes [27], we established upper bounds on the charge Q. The allowed values must be consistent with the existence of an event horizon, ensuring that the solution represents a black hole spacetime. In our model [27], the existence of a horizon is determined by the values of the parameters c_O, α and the charge Q. In [27], we show the variation of the upper bound on Q with the symmergent parameter c_O for two cases, namely: $\alpha = 1.10$ (AdS case) and $\alpha = 0.90$ (dS case). Specifically, for the AdS case maximum allowed value of the charge is around $Q_h = 1.48M$ and for the dS case the upper bound reduces to around $Q_h = 1.34M$ for $c_O = 0.90$ where we use the label Q_h for Q upper bound derived from the horizon formation which exhibits a mild dependence on c_O is mild.In addition, the photon sphere condition yields an analytic upper bound on the electric charge, however it is less stringent than the horizon condition.

The most stringent observational constraints on the Symmergent parameter c_O arise from black-hole shadow measurements. We compared the theoretical shadow radius with the EHT results for Sgr A* and M87* at the 1σ confidence level. Our analysis indicates that very small values of c_O are ruled out, since they yield shadow sizes below the observed bands. As c_O increases, the shadow radius grows and rapidly saturates to an asymptotic value consistent with the data. The admissible ranges of c_O inferred from the EHT observations are presented for fixed charge values, and we find that the dependence on $\hat{\alpha}$ remains weak. For example, when $Q/M = 0.05$ and $\alpha = 0.90$, the shadow constraints require

$$\log_{10}\left(\tfrac{c_O}{M^2}\right) \gtrsim 39.6 \quad \text{for Sgr A*},$$

$$\log_{10}\left(\tfrac{c_O}{M^2}\right) \gtrsim 45.1 \quad \text{for M87*}.$$

No significant upper bound emerges in the explored domain, as the shadow curves flatten at large c_O. In this work, we adopt representative benchmark values of c_O to illustrate the functional dependence of quasinormal modes and greybody factors. Our focus is on identifying qualitative trends and parameter sensitivities rather than performing a fully constrained parameter scan. The quantitative bounds on c_O, already established from shadow measurements in Ref. [27], provide the observational foundation, while the present analysis highlights the near-horizon behavior and dynamical imprints of charged Symmergent black holes.

In this study, we use benchmark values of c_O to illustrate QNM and greybody behavior, with the quantitative constraints already established in our earlier work [27]. We carry out the analyses in the subsequent sections by taking into account the allowed ranges of the model parameters.

3 Perturbations and quasinormal modes

In this section, we focus on the analysis of massless scalar and vector perturbations within the framework of the black hole metric defined in Eq. (12). For the sake of simplicity, we assume that the test field, whether a scalar field or a vector field, exerts a negligible influence on the black hole spacetime, meaning that the back reaction of the field on the spacetime geometry is insignificant [49,149]. This assumption allows us to treat the perturbations as propagating on a fixed background metric without needing to consider the complex, coupled dynamics that would arise if the back reaction were significant.

To investigate the QNMs associated with these perturbations, we derive Schrödinger-like wave equations tailored to each case by imposing the relevant conservation relations on the background spacetime. For scalar fields, this process results in equations of the Klein–Gordon type, which describe how the scalar perturbations evolve in the curved spacetime. For electromagnetic (vector) fields, the corresponding wave equations are derived from Maxwell's equations, governing the dynamics of electromagnetic perturbations. These equations encapsulate the key physical properties of the perturbations, such as their frequencies and damping rates, which are essential for determining the QNMs.

The QNMs are calculated using the Padé-averaged 6th-order WKB approximation method, a semi-analytical tech-

nique that is particularly effective for evaluating the frequencies and decay rates of perturbations in black hole spacetimes. The WKB method is well-suited for handling wave equations with a potential barrier, as is typical in the context of black hole perturbations. By employing this method, we can obtain accurate estimates of the QNMs, which provide insights into the stability and dynamical response of the black hole to perturbations.

Our analysis specifically focuses on axial perturbations. To describe these perturbations, we express the perturbed metric as shown in the following way [149]

$$\begin{aligned} ds^2 = &-g_{tt}dt^2 + r^2 d\theta^2 + g_{rr}dr^2 \\ &+r^2\sin^2\theta\ (d\phi - p_1(t,r,\theta) \\ &dt - p_2(t,r,\theta)\,dr - p_3(t,r,\theta)\,d\theta)^2\ , \end{aligned} \tag{13}$$

where the functions $p_1(t,r,\theta)$, $p_2(t,r,\theta)$, and $p_3(t,r,\theta)$ characterize the perturbations in the black hole spacetime. These functions represent deviations from the static and spherically symmetric background metric, with $g_{tt} = h(r)$ and $g_{rr} = 1/h(r)$ serving as the zeroth-order terms in the perturbative expansion. These zeroth-order terms correspond to the unperturbed black hole metric, while the functions p_i encode the effects of the axial perturbations.

Through this approach, we systematically study the impact of massless scalar and vector perturbations on the black hole spacetime, providing a deeper understanding of the behavior and characteristics of QNMs in this context. This analysis is crucial for exploring the stability of black holes and the nature of gravitational and electromagnetic waves in curved spacetime, offering valuable insights into the fundamental properties of black hole physics.

3.1 Massless scalar perturbation

We begin by considering a massless scalar field Φ in the vicinity of a CSBH, governed by the equation $\Box\Phi = 0$, which describes the motion of the scalar field assuming negligible backreaction. The corresponding Klein–Gordon equation in the CSBH spacetime takes the form

$$\begin{aligned} &\frac{1}{r^2\sqrt{g_{tt}g_{rr}^{-1}}}\left[r^2\sqrt{g_{tt}g_{rr}^{-1}}\Phi_{,r}\right]_{,r} \\ &+\frac{g_{tt}}{r^2\sin\theta}\left(\sin\theta\Phi_{,\theta}\right)_{,\theta} + \frac{g_{tt}}{r^2\sin^2\theta}(\Phi)_{,\phi\phi} - (\Phi)_{,tt} = 0. \end{aligned} \tag{14}$$

The angular structure of this equation suggests that the appropriate basis functions for the polar orientation are the associated Legendre polynomials $P_l^m(\cos\theta)$, which satisfy the relation

$$\begin{aligned} &\frac{1}{\sin\theta}\frac{d}{d\theta}\left(\sin\theta\frac{dP_l^m(\cos\theta)}{d\theta}\right) - \frac{m^2}{\sin^2\theta}\Phi \\ &= -l(l+1)P_l^m(\cos\theta). \end{aligned} \tag{15}$$

After separating the ϕ-dependent part of the equation using $\partial_\phi^2\Phi = -m^2\Phi$, we express the scalar perturbation as a multipole expansion:

$$\begin{aligned} \Phi(t,r,\theta,\phi) = &\frac{1}{r}\sum_{l,m} \\ &\sqrt{\frac{(2l+1)}{4\pi}\frac{(l-m)!}{(l+m)!}}\psi_s(t,r)e^{im\phi}P_l^m(\cos\theta), \end{aligned} \tag{16}$$

where l and m represent the polar and azimuthal indices, respectively [49,151]. The function $\psi_s(t,r)$ is the radial time-dependent wave function and the index "s" stands for scalar.

Substituting this expansion into the Klein–Gordon equation leads to the stationary Schrödinger-like equation for the radial part:

$$\partial_{r_*}^2\psi(r_*)_{sl} + \omega^2\psi(r_*)_s = V_s(r)\psi(r_*)_s, \tag{17}$$

where r_* is the tortoise coordinate.

The term $V_s(r)$ represents the effective potential, given by

$$\begin{aligned} V_s(r) &= |g_{tt}|\left(\frac{l(l+1)}{r^2} + \frac{1}{r\sqrt{|g_{tt}|g_{rr}}}\frac{d}{dr}\sqrt{|g_{tt}|g_{rr}^{-1}}\right) \\ &= h(r)\left(\frac{l(l+1)}{r^2} + \frac{1}{r}\frac{d}{dr}h(r)\right). \end{aligned} \tag{18}$$

Here, l corresponds to the multipole moment of the black hole's QNMs, and ω represents the frequency of these modes, which is determined from $\partial_t^2\psi_s(t,r_*) = -\omega^2\psi_s(t,r_*)$. The wavefunction $\psi(r_*)_s$ thus describes behaviour of the scalar QNMs of the CSBH [49,149].

This formalism shows how scalar field perturbations evolve in the spacetime around CSBHs, with the effective potential and tortoise coordinate playing key roles in shaping the dynamics of the QNMs. The diagonal and static nature of the CSBH metric facilitates the straightforward definition of the QNM frequencies, which are essential for understanding the behavior of the scalar perturbations in these exotic spacetimes.

Although in our investigation primarily focuses on massless scalar perturbation, the scalar field can be massive also. The master wave equation with the effective potentials used

here follows the standard Regge-Wheeler/Zerilli and Chandrasekhar formulations. In such a scenario, the potential takes the form [42,44,50–52,149,150,174]:

$$V_{sm}(r) = h(r)\left(\frac{l(l+1)}{r^2} + \frac{1}{r}\frac{d}{dr}h(r) + \mu^2\right), \tag{19}$$

where μ is the mass of the scalar field. Usually, for massive scalar field the oscillation frequency of ring-down GWs increases and the damping rate decreases. In this work, we shall consider $\mu = 0$ i.e., a massless scalar field.

3.2 Massless vector or electromagnetic perturbation

Following the analysis of scalar perturbations, we now turn to the study of massless vector perturbations, specifically focusing on electromagnetic perturbations. The tetrad formalism proves to be a useful approach in analyzing these perturbations, as it allows the projection of the curved metric $g_{\mu\nu}$ onto the flat metric $\eta_{\bar{\mu}\bar{\nu}}$ using the vierbein $e^{\bar{\mu}}_{\mu}$. In this formalism, the relationship between the curved and flat metrics is given by $g_{\mu\nu} = e^{\bar{\mu}}_{\mu}\eta_{\bar{\mu}\bar{\nu}}e^{\bar{\nu}}_{\nu}$, where the indices $\mu, \nu, \ldots$ refer to the curved spacetime, and $\bar{\mu}, \bar{\nu}, \ldots$ refer to the flat spacetime. The vierbeins satisfy several key relations $e^{\bar{\mu}}_{\mu}e^{\mu}_{\bar{\nu}} = \delta^{\bar{\mu}}_{\bar{\nu}}$, $e^{\bar{\mu}}_{\mu}e^{\nu}_{\bar{\mu}} = \delta^{\nu}_{\mu}$ and $e^{\bar{\mu}}_{\mu} = g_{\mu\nu}\eta^{\bar{\mu}\bar{\nu}}e^{\nu}_{\bar{\nu}}$ enabling us to express a given vector S_μ and a tensor $P_{\mu\nu}$ in terms of their flat-spacetime counterparts.

The electromagnetic field strength tensor $F_{\bar{\mu}\bar{\nu}}$ is governed by the Jacobi identity $\partial_{[\bar{\mu}}F_{\bar{\nu}\bar{\rho}]} = 0$, leading to a set of constraints on the vector perturbations. Using these equations, we derive a two-derivative motion equation for the vector perturbations, expressed as

$$\left[\sqrt{g_{tt}g_{rr}^{-1}}\left(r\sqrt{g_{tt}}\,\mathcal{F}\right)_{,r}\right]_{,r} + \frac{g_{tt}\sqrt{g_{rr}}}{r}\left(\frac{\mathcal{F}_{,\theta}}{\sin\theta}\right)_{,\theta}\sin\theta - r\sqrt{g_{rr}}\,\mathcal{F}_{,tt} = 0, \tag{20}$$

where $\mathcal{F} = F_{\bar{t}\bar{\phi}}\sin\theta$. Unlike scalar perturbations, the angular part of this equation suggests that the appropriate basis functions are the Gegenbauer polynomials $P_l(\cos\theta| - 1)$, which satisfy the differential equation

$$\sin\theta\frac{d}{d\theta}\left(\frac{1}{\sin\theta}\frac{dP_l(\cos\theta|-1)}{d\theta}\right) = -l(l-1)P_l(\cos\theta|-1). \tag{21}$$

The vector wavefunction $\mathcal{F}(t, r, \theta, \phi)$ can then be expanded in terms of these polynomials as

$$\mathcal{F}(t, r, \theta, \phi) = \sum_l \psi_{em}(t, r)\frac{dP_l(\cos\theta|-1)}{\sin\theta d\theta}, \tag{22}$$

leading to the equation for the radial part of the vector perturbations:

$$\left[\sqrt{g_{tt}g_{rr}^{-1}}\left(r\sqrt{g_{tt}}\,\psi_{em}\right)_{,r}\right]_{,r} + \omega^2 r\sqrt{g_{rr}}\,\psi_{em} - \frac{1}{r}g_{tt}\sqrt{g_{rr}}\,l(l+1)\,\psi_{em} = 0. \tag{23}$$

Here ψ_{em} is the wave function associated with the electromagnetic perturbation. This equation mirrors the form of the scalar perturbation equation, with the key difference being the absence of a derivative term in the effective potential for vector perturbations.

By defining the tortoise coordinate r_* as in the scalar case, the vector perturbations obey the stationary Schrödinger equation

$$\partial^2_{r_*}\psi_{em}(r_*) + \omega^2\psi_{em}(r_*) = V_{em}(r)\psi_{em}(r_*), \tag{24}$$

where the effective potential for electromagnetic perturbations is

$$V_{em}(r) = g_{tt}\frac{l(l+1)}{r^2} = h(r)\frac{l(l+1)}{r^2}. \tag{25}$$

This potential differs from that of scalar perturbations, as it lacks the derivative term associated with the metric function $h(r)$.

While these vector perturbations can be identified with the electromagnetic field, the broader symmergent gravity framework predicts the existence of additional massless particles, which may not interact with known particles through non-gravitational forces. These could include massless scalar fields or massless (dark) photons, which could significantly influence gravitational wave emissions. The presence of such particles in the symmergent particle spectrum could lead to observable deviations in the dynamics of gravitational waves and other astrophysical phenomena [16,22,23].

3.3 Gravitational perturbations

In this subsection, we analyze axial gravitational perturbations to derive a Schrödinger-like wave equation characterized by an effective potential V_g. This potential will be fundamental for computing the QNMs, as detailed in subsequent part of the study. Axial perturbations, which are distinguished by their transformation properties under parity, are particularly important for studying the gravitational stability and dynamics of compact astrophysical objects within general relativity. Therefore, for the completeness of the study, apart from scalar and electromagnetic perturbations, we are also considering gravitational perturbation to calculate QNMs in this study.

Notably, as shown in Ref. [148], for an anisotropic fluid undergoing axial perturbations, the axial components of the

perturbed energy–momentum tensor vanish. This crucial simplification allows the use of the tetrad formalism, reducing the condition for perturbations to:

$$R_{(a)(b)} = 0, \tag{26}$$

where $R_{(a)(b)}$ denotes the Ricci tensor components expressed in the tetrad frame.

Focusing explicitly on the $\theta\phi$ and $r\phi$ components of this equation, one obtains the following coupled equations, originally derived in Ref. [149]:

$$\left[r^2\sqrt{|g_{tt}|\,g_{rr}^{-1}}\,(a_{2,\theta} - a_{3,r})\right]_{,r} = r^2\sqrt{|g_{tt}|^{-1}\,g_{rr}}\,(a_{1,\theta} - a_{3,t})_{,t}, \tag{27}$$

$$\left[r^2\sqrt{|g_{tt}|\,g_{rr}^{-1}}\,(a_{3,r} - a_{2,\theta})\sin^3\theta\right]_{,\theta} = \frac{r^4\sin^3\theta}{\sqrt{|g_{tt}|\,g_{rr}}}(a_{1,r} - a_{2,t})_{,t}. \tag{28}$$

Next, we simplify the above equations by employing the method of separation of variables. We assume the perturbation function can be decomposed as:

$$\mathcal{F}_g(r,\theta) = \mathcal{F}_g(r)\,Y(\theta), \tag{29}$$

where the angular function $Y(\theta)$ satisfies the modified differential equation:

$$\frac{d}{d\theta}\left(\sin^{-3}\theta\frac{dY}{d\theta}\right) = -\left[l(l+1) - 2\right]\frac{Y}{\sin^3\theta}. \tag{30}$$

Here, l is the angular momentum quantum number. The presence of the factor $l(l+1)-2$ distinguishes axial perturbations from the standard spherical harmonic equation, reflecting the unique angular dependence of these modes.

By substituting this ansatz into Eqs. (27) and (28), and after appropriate algebraic manipulation, the system simplifies into a radial equation resembling the familiar Schrödinger form:

$$\frac{d^2\psi_g}{dr_*^2} + \omega^2\psi_g = V_g(r)\,\psi_g, \tag{31}$$

where we introduced the radial wavefunction transformation $\psi_g r = \mathcal{F}_g$, and r_* denotes the tortoise coordinate, defined by:

$$dr_* = \sqrt{\frac{g_{rr}}{|g_{tt}|}}\,dr. \tag{32}$$

The effective gravitational potential $V_g(r)$ appearing in the Schrödinger-like equation is explicitly given by:

$$V_g(r) = |g_{tt}|\left[\frac{2}{r^2}\left(\frac{1}{g_{rr}} - 1\right) + \frac{l(l+1)}{r^2} - \frac{1}{r\sqrt{|g_{tt}|\,g_{rr}}}\frac{d}{dr}\left(\sqrt{|g_{tt}|\,g_{rr}^{-1}}\right)\right]. \tag{33}$$

This formula explicitly illustrates how the background metric, represented by g_{tt} and g_{rr}, directly influences the gravitational perturbations. The resulting potential is crucial to examining how compact astrophysical objects respond to gravitational perturbations, enabling the detailed exploration of quasinormal modes and their implications in the subsequent analysis.

3.4 Behaviour of the perturbation potentials

Here, we briefly explore the characteristics of the perturbation potentials associated with the black hole under consideration. The perturbation potential plays a crucial role in determining the QNMs of the black hole, as the nature of the potential directly influences the frequencies and damping rates of these oscillatory modes. By analyzing the behavior of the potential, we can gain a preliminary understanding of the QNMs and their dependence on various parameters.

The first and second panels of Fig. 1 illustrate the scalar potential for different values of the multipole moment l with $\alpha = 0.9$ and $\alpha = 1.1$. As expected, the peak value of the potential increases with an increase in l. This trend is consistent with the understanding that higher multipole moments correspond to more complex angular dependencies in the perturbation, leading to a stronger potential barrier. The rise in the potential peak with increasing l indicates that the black hole is more resistant to perturbations with higher angular momentum, which will likely result in QNMs with higher frequencies and shorter lifetimes. This is because the potential barrier effectively traps the perturbation closer to the black hole, leading to faster decay and higher oscillation frequencies.

In the third panel of Fig. 1, we examine the variation of the scalar potential with respect to the model parameter α. The potential curve rises significantly as α increases, indicating that this parameter has a substantial impact on the behavior of the potential. The parameter α likely represents a characteristic of the modified gravity model or an additional field interacting with the black hole spacetime. The increase in the potential with α suggests that higher values of α make the black hole more resistant to scalar perturbations, potentially leading to higher QNM frequencies and faster damping rates. This observation underscores the sensitivity of the QNMs to the underlying model parameters, highlighting the impor-

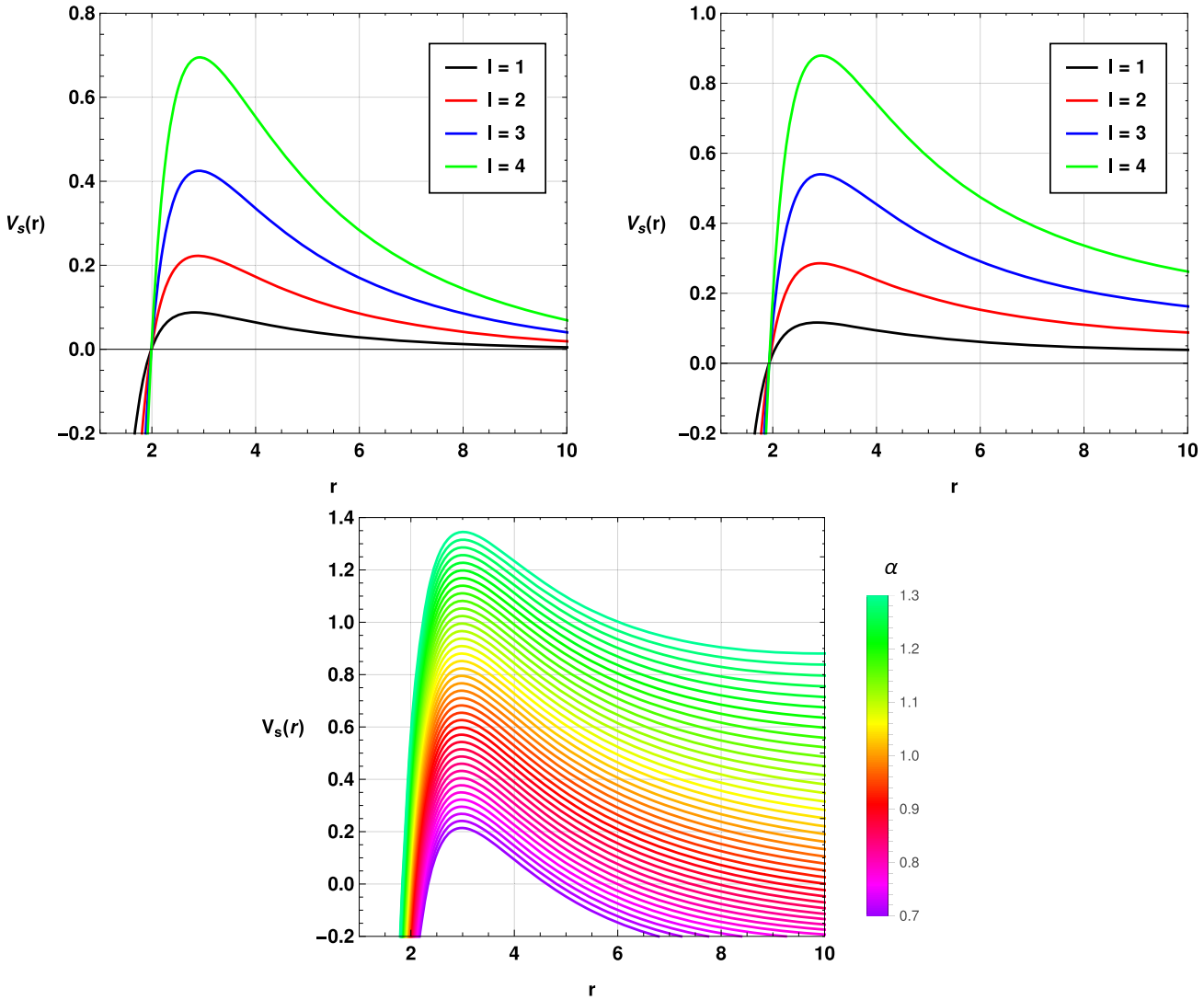

Fig. 1 Variation of the scalar potential $V_s(r)$ of CSBH with the radial distance r for different values of the multipole moment l with $M = 1$, $G = 1$, $\alpha = 0.9$, $Q = 0.4$ and $c_O = 0.3$ (first panel), with $M = 1$, $G = 1, \alpha = 1.1$, $Q = 0.4$ and $c_O = 0.3$ (second panel) and for different values of α with $l = 4$, $M = 1$, $Q = 0.1$ and $c_O = 0.15$ (third panel)

tance of understanding how these parameters influence the perturbation dynamics.

Moving to Fig. 2, the first panel displays the variation of the scalar potential concerning the parameter c_O. The potential curve shows a rapid increase for very small positive values of c_O, while for negative values close to zero, the potential decreases drastically. As c_O becomes more positive or more negative, the potential tends to stabilize towards a central value. This behavior indicates that c_O exerts a complex influence on the potential, possibly related to the asymptotic behavior of the spacetime or the nature of the coupling between the black hole and the scalar field. The rapid changes in the potential for small values of c_O suggest that even slight variations in this parameter can significantly alter the QNMs, making it a critical factor in the stability analysis of the black hole.

The second panel of Fig. 2 shows the variations of the potential with respect to the charge Q of the black hole. The black hole charge has a pronounced effect on the potential behavior. As Q increases, the peak value of the potential rises significantly, and the radius r corresponding to the maximum of the potential shifts closer to the event horizon. This shift suggests that the presence of charge enhances the black hole's ability to trap perturbations near the horizon, leading to higher QNM frequencies. The charge Q has a significant impact on the structure of the potential. With an increase in the value of the charge Q, both the height and width of the potential increase and the peak of the potential shifts towards

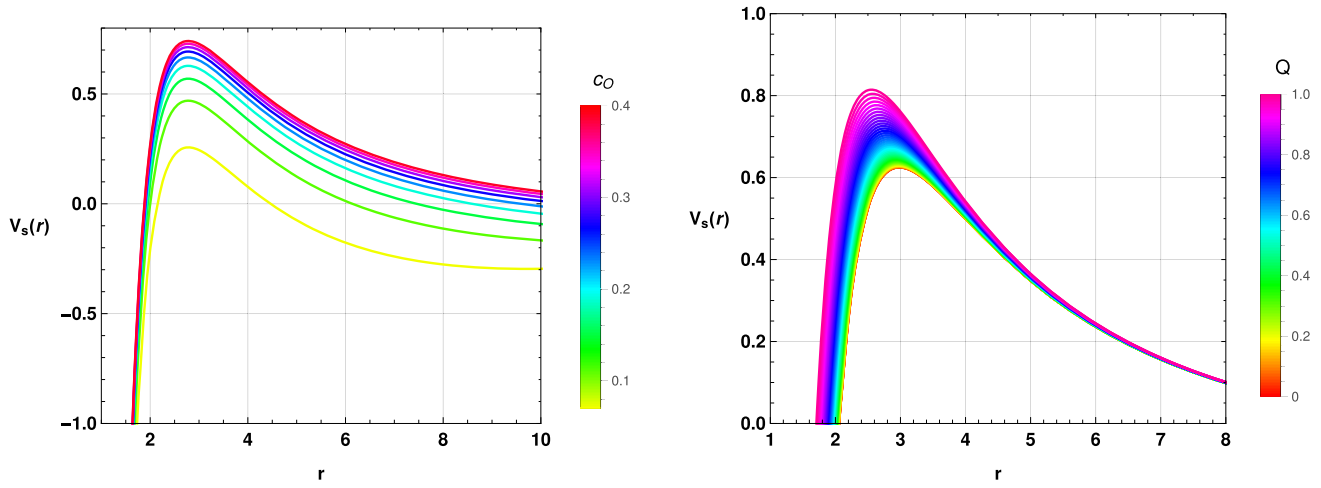

Fig. 2 Variation of the scalar potential $V_s(r)$ of CSBH with the radial distance r with $M = 1$, $G = 1$, $\alpha = 0.90$ and $l = 4$. On the left panel $Q = 0.7$. On the right panel $c_{\mathrm{O}} = 0.2$

the event horizon, which may result in a more complex QNM spectrum.

We have also plotted similar curves for the electromagnetic potential in Figs. 3 and 4, considering different values of the model parameters and multipole moments. The qualitative behavior of the electromagnetic potential curves is similar to that observed for the scalar potential. However, a notable difference is that the potential values for the scalar perturbation are generally higher than those for the electromagnetic perturbation. This difference suggests that the scalar field experiences a stronger interaction with the black hole spacetime, leading to higher potential barriers. Consequently, we expect the QNM spectrum for scalar perturbations to have higher frequencies and shorter lifetimes compared to electromagnetic perturbations. The lower potential values for the electromagnetic case imply that the QNMs associated with electromagnetic perturbations might exhibit lower frequencies and longer damping times, indicating a more gradual decay of these modes.

In Figs. 5 and 6, we have shown the behaviour of the gravitational potential with respect to r for different values of the model parameters. One may note that the variation of the potential with respect to the model parameters is similar to the cases of scalar perturbation and electromagnetic perturbation. However, the peak value of the potential appears to be lower in the case of gravitational perturbations.

The analysis of the perturbation potential provides valuable insights into the nature of the QNMs for scalar, electromagnetic and gravitational perturbations. The variations in the potential with respect to parameters such as the multipole moment l, the model parameter α, the coupling parameter c_{O}, and the black hole charge Q reveal how sensitive the QNMs are to these factors. This understanding is crucial for predicting the stability and dynamical response of black holes to perturbations, particularly in the context of different gravity models or in the presence of additional fields. One may note that with $Q = 0$, one can easily obtain the corresponding potentials discussed in Ref. [35]. However, we have noticed that the charge of the black hole i.e. Q has a noticeable impact on the QNMs spectrum as predicted by the variation of the corresponding potential. In the presence of Q, the peak value of the potential increases and the variation is not similar to that of the Reissner–Nordström black hole. Hence, the QNMs spectrum seems to be different from that of a standard Reissner–Nordström black hole.

3.5 Time-domain profile and quasinormal modes

To begin, let us first examine the time-domain profile of the scalar field before delving into the determination of QNMs. In the preceding section, we undertook extensive numerical computations to characterize the QNMs, thoroughly analyzing how these modes depend on the model parameters Q, α, and c_{O}. Our approach involved solving the perturbation equations in the frequency domain, which provided insights into the oscillatory behavior and damping times of the QNMs. However, frequency-domain analysis alone does not capture the full temporal evolution of the perturbations. Thus, in the subsequent section, our focus shifts towards understanding the time-domain behavior of both scalar and electromagnetic perturbations. This involves generating temporal profiles that illustrate how these fields evolve with time after an initial disturbance. To achieve this, we employ a time-domain integration framework based on the methodology proposed by Gundlach et al. [160], which is well-suited for capturing the full dynamical evolution of perturbations. By applying this technique, we can observe the decay patterns and the late-time behavior of the perturbations, offering a complemen-

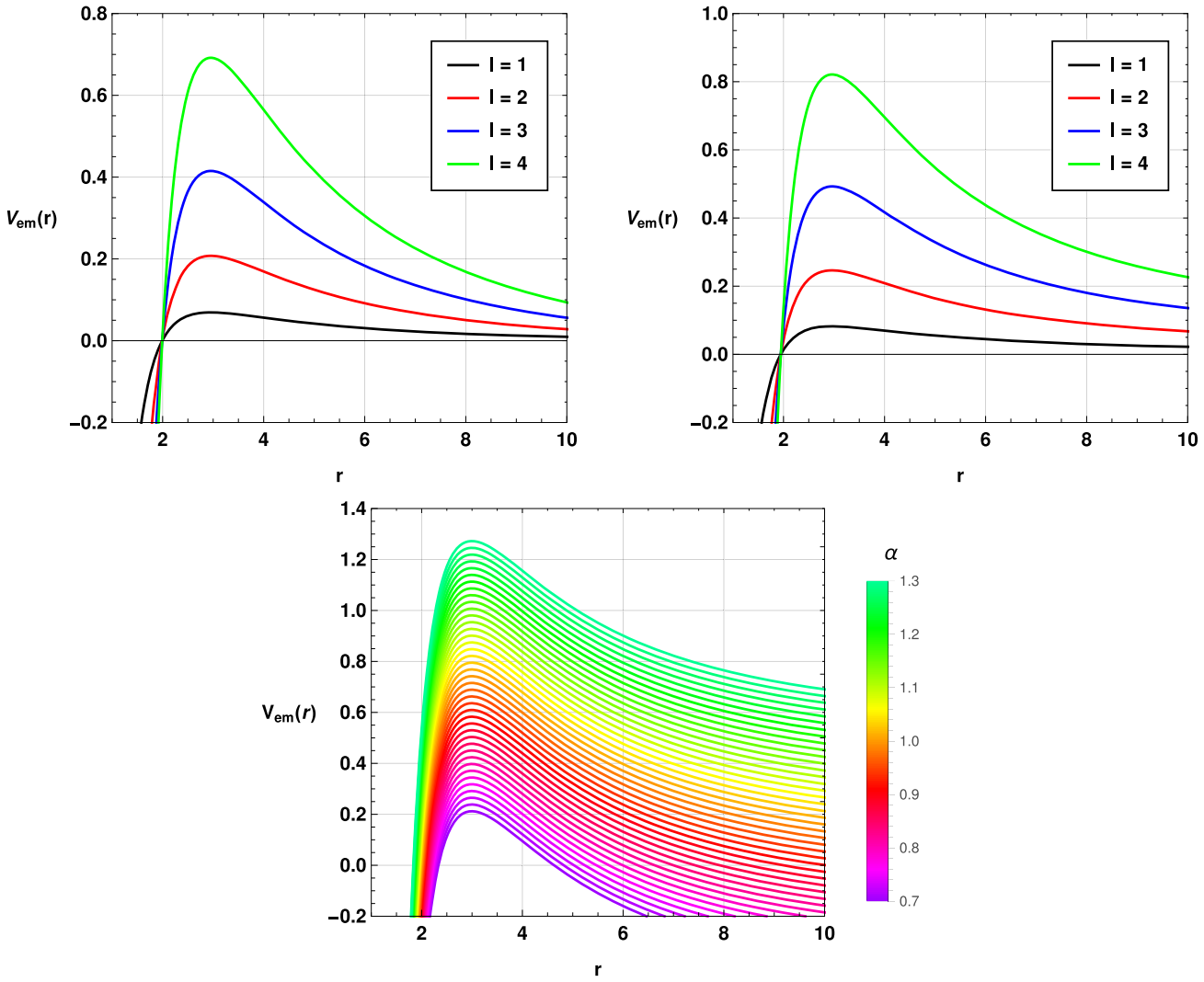

Fig. 3 Variation of electromagnetic potential $V_{em}(r)$ of CSBH with the radial distance r for different values of the multipole moment l with $M = 1$, $G = 1$, $\alpha = 0.9$, $Q = 0.35$ and $c_{\mathrm{O}} = 0.4$ (first panel), with $M = 1$, $G = 1$, $\alpha = 1.1$, $Q = 0.35$ and $c_{\mathrm{O}} = 0.4$ (second panel) and for different values of α with $M = 1$, $l = 4$, $Q = 0.1$ and $c_{\mathrm{O}} = 0.15$

tary perspective to the frequency-domain analysis. This dual approach not only helps in verifying the consistency of our results but also provides a more comprehensive understanding of the dynamical properties of the perturbations in the given gravitational background.

Now, to proceed with the time domain investigation, we at first define $\psi(r_*, t) = \psi(i\Delta r_*, j\Delta t) = \psi_{i,j}$ and $V(r(r_*)) = V(r_*, t) = V_{i,j}$. Using this expression, we write

$$\frac{\psi_{i+1,j} - 2\psi_{i,j} + \psi_{i-1,j}}{\Delta r_*^2} - \frac{\psi_{i,j+1} - 2\psi_{i,j} + \psi_{i,j-1}}{\Delta t^2} - V_i\psi_{i,j} = 0. \tag{34}$$

In this scheme, we use the inittial conditions $\psi(r_*, t) = \exp\left[-\frac{(r_* - k_1)^2}{2\sigma^2}\right]$ and $\psi(r_*, t)|_{t<0} = 0$ (note that k_1 and σ are the median and width of the initial wave-packet in the analysis scheme). By utilising these expressions, one can obtain the time evolution of the scalar perturbation as shown below:

$$\psi_{i,j+1} = -\psi_{i,j-1} + \left(\frac{\Delta t}{\Delta r_*}\right)^2 (\psi_{i+1,j} + \psi_{i-1,j}) + \left(2 - 2\left(\frac{\Delta t}{\Delta r_*}\right)^2 - V_i\Delta t^2\right)\psi_{i,j}. \tag{35}$$

One can obtain the required time domain profiles numerically by using this iteration scheme along with a suitable

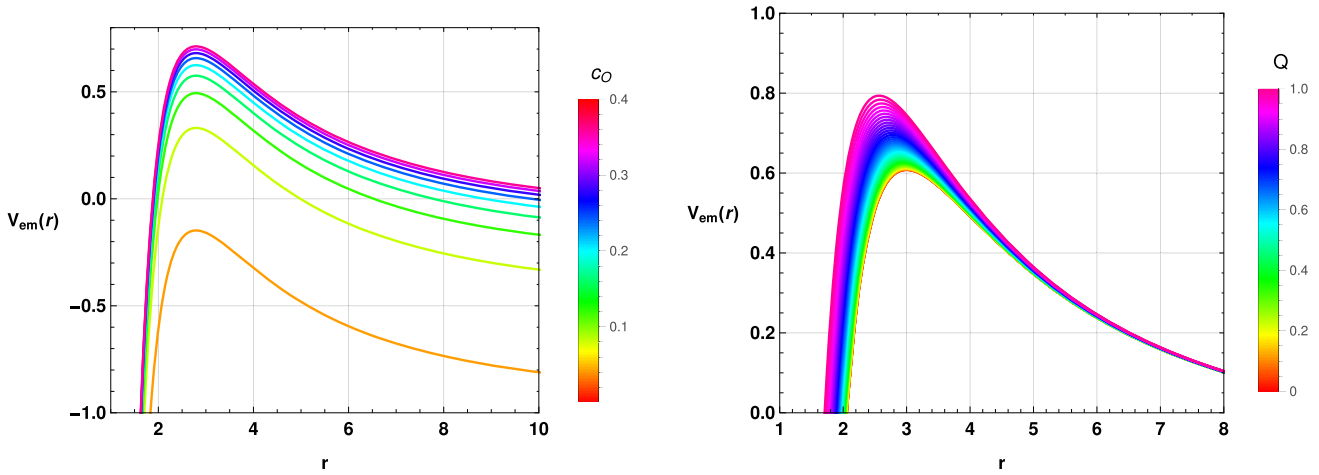

Fig. 4 Variation of electromagnetic potential $V_{em}(r)$ of CSBH with the radial distance r with $M = 1$, $l = 4$ and $\alpha = 0.90$. On the left panel $Q = 0.7$. On the right panel $c_O = 0.2$

fixed value of the fraction $\frac{\Delta t}{\Delta r_*}$. Here a suitable value implies that the ratio $\frac{\Delta t}{\Delta r_*}$ must be less than 1 in order to satisfy the Von Neumann stability condition.

The time-domain profiles of scalar, electromagnetic and gravitational perturbations provide important insights into the dynamic behavior of these fields in black hole spacetimes. The left panel of Fig. 7 presents the temporal profile of scalar perturbations, while the second panel shows that of electromagnetic perturbations and the third panel shows that of gravitational perturbations. The chosen parameters include an overtone number of $n = 0$, with $\alpha = 0.9$, $Q = 0.3$, and $c_O = 0.4$, while the multipole moment l is varied. Both profiles reveal that an increase in l leads to higher frequencies of oscillations. However, the decay rates behave differently for scalar, electromagnetic and gravitational perturbations. In the case of scalar perturbations, the decay rate increases significantly as l grows, meaning that higher multipole moments correspond to faster damping. In contrast, the decay rate for electromagnetic perturbations as well as gravitational perturbations seems to show only a slight variation with increasing l. Additionally, scalar perturbations tend to damp out faster than the other two cases, implying that scalar fields are more sensitive to perturbations and exhibit quicker stabilization in the black hole environment.

Figure 8 further explores the time-domain profiles by varying the model parameter α, keeping the overtone number $n = 0$, multipole moment $l = 1$, $Q = 0.3$, and $c_O = 0.4$ fixed. Similar to the previous case, the decay rate for scalar perturbations is consistently greater than that for electromagnetic and gravitational perturbations. This suggests that α exerts a more pronounced influence on the scalar field. As the value of α increases, both the oscillation frequency and decay rate are affected, but the damping of scalar perturbations remains more rapid than that of electromagnetic and gravitational perturbations. The scalar field tends to dissipate faster, reflecting its stronger interaction with the black hole geometry compared to electromagnetic fields. In the third panel, we have shown the time domain profiles for gravitational perturbation. One may note that for this case, we have considered $l = 2$ which is the fundamental case.

Figure 9 examines the effects of the parameter c_O on the time-domain profiles. Here, for small values of time t, all the three perturbations exhibit very similar profiles, with minimal differences in their oscillation patterns. However, as time progresses, variations in oscillation frequencies become more noticeable, particularly for larger values of t. Despite these differences, the damping rates for both types of perturbations appear relatively unaffected by changes in c_O, suggesting that this parameter influences the frequency of oscillations more than the rate at which the perturbations decay. For the range of c_O values considered, the impact on damping seems marginal, indicating that c_O primarily affects the oscillatory dynamics rather than the overall stability.

Finally, in Fig. 10, the time-domain profiles are plotted with varying values of the charge parameter Q. The results indicate that the black hole charge has a noticeable effect on the oscillation frequency for all the three perturbations. As Q increases, the oscillation frequencies increase, suggesting that a more highly charged black hole causes perturbations to oscillate more rapidly. The damping rate, however, increases only slightly for both types of perturbations, implying that while the charge of the black hole influences the oscillatory behavior, it has a relatively minor impact on the overall rate at which the perturbations decay. This finding highlights that the black hole charge primarily affects the dynamic response of the system without drastically altering its stability over time.

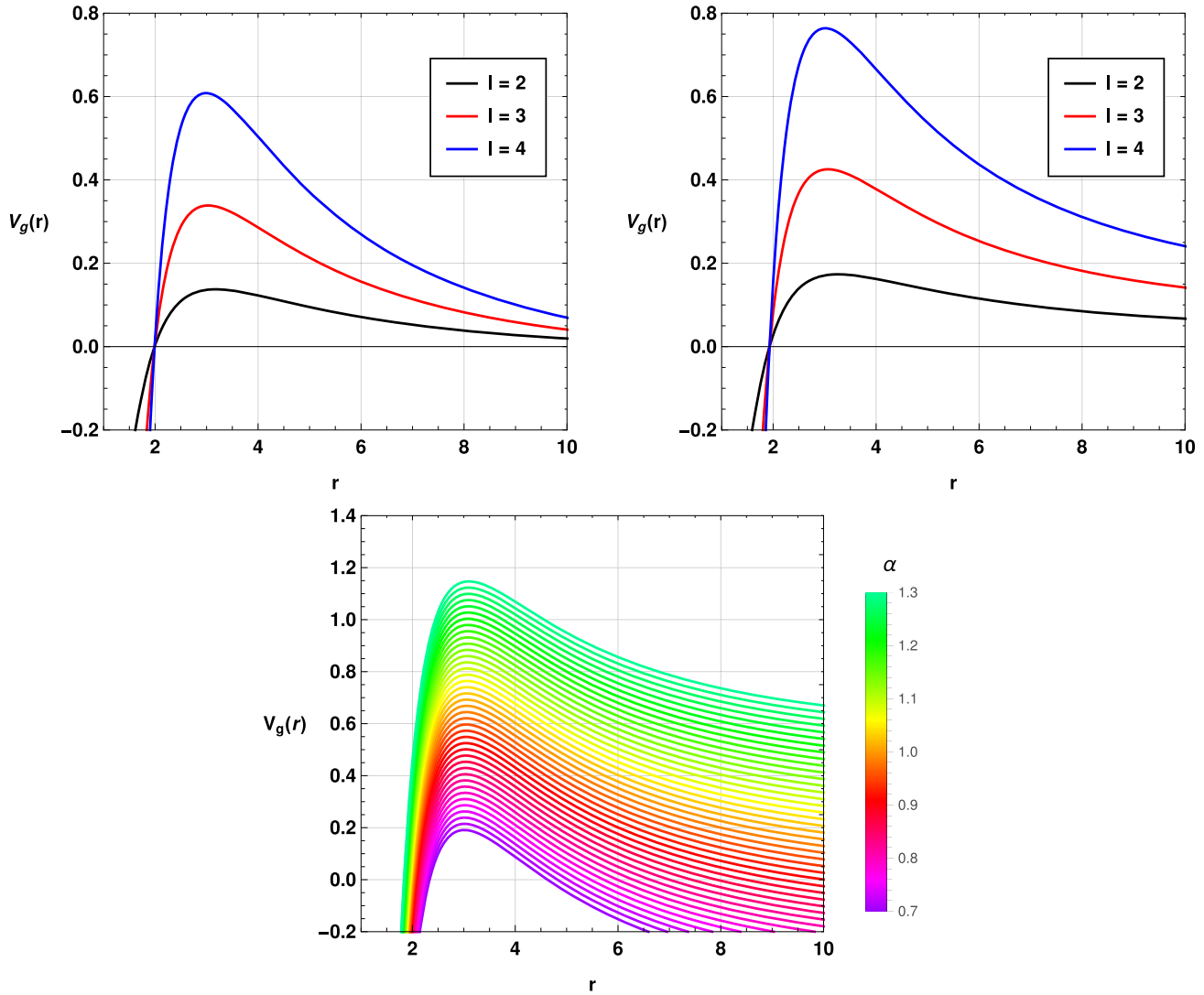

Fig. 5 Variation of gravitational potential $V_g(r)$ of CSBH with the radial distance r for different values of the multipole moment l with $M = 1$, $G = 1$, $\alpha = 0.9$, $Q = 0.35$ and $c_{\mathrm{O}} = 0.4$ (first panel), with $M = 1$, $G = 1$, $\alpha = 1.1$, $Q = 0.35$ and $c_{\mathrm{O}} = 0.4$ (second panel) and for different values of α with $M = 1$, $l = 4$, $Q = 0.1$ and $c_{\mathrm{O}} = 0.15$ (third panel)

The time-domain profiles of scalar, electromagnetic and gravitational perturbations reveal key differences in how these fields evolve over time in the presence of a black hole. Scalar perturbations generally exhibit higher decay rates and faster damping than electromagnetic and gravitational perturbations, making them more responsive to changes in the black hole's parameters, such as the multipole moment l, the model parameter α, and the charge Q. These results provide a deeper understanding of the dynamics of black hole perturbations and the influence of various physical parameters on the behavior of QNMs.

3.6 WKB method with Padé approximation for quasinormal modes

In this study, we aim to estimate the QNMs of the black holes by employing the Wentzel-Kramers-Brillouin (WKB) method, a widely recognized approximation technique in the field of black hole perturbation theory. Initially introduced by Schutz and Will [156], the WKB method provides a first-order approximation for calculating QNMs. However, despite its utility, the method is known to exhibit certain limitations, including a higher degree of error in some cases. To address these limitations, researchers have developed higher-order WKB approximations, significantly improving the accuracy of QNM calculations [157–159]. Our work

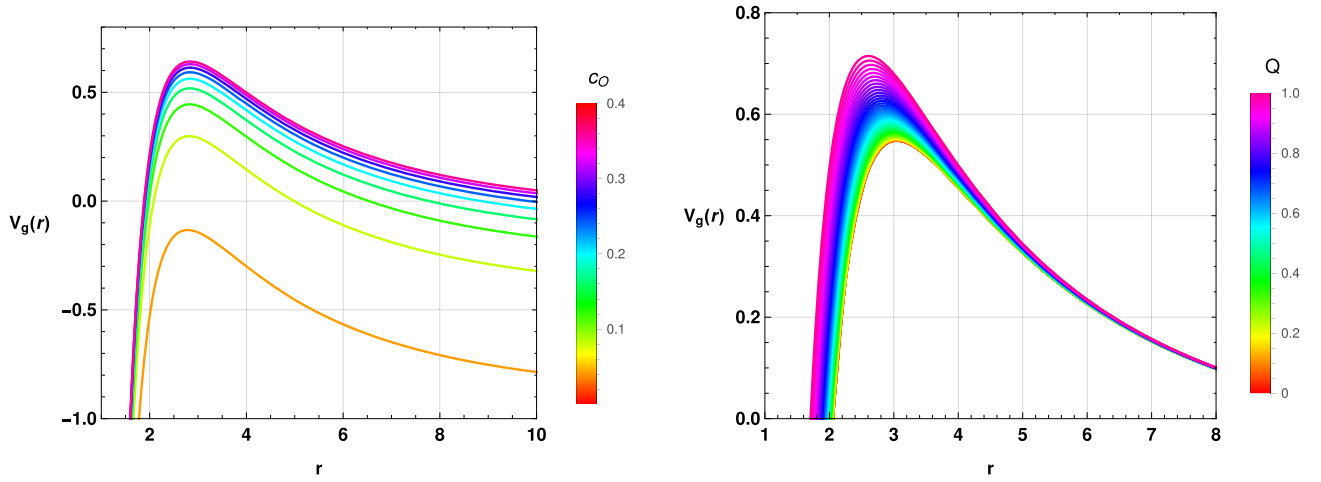

Fig. 6 Variation of gravitational potential $V_g(r)$ of CSBH with the radial distance r with $M = 1, l = 4$ and $\alpha = 0.90$. On the left panel $Q = 0.7$. On the right panel $c_O = 0.2$

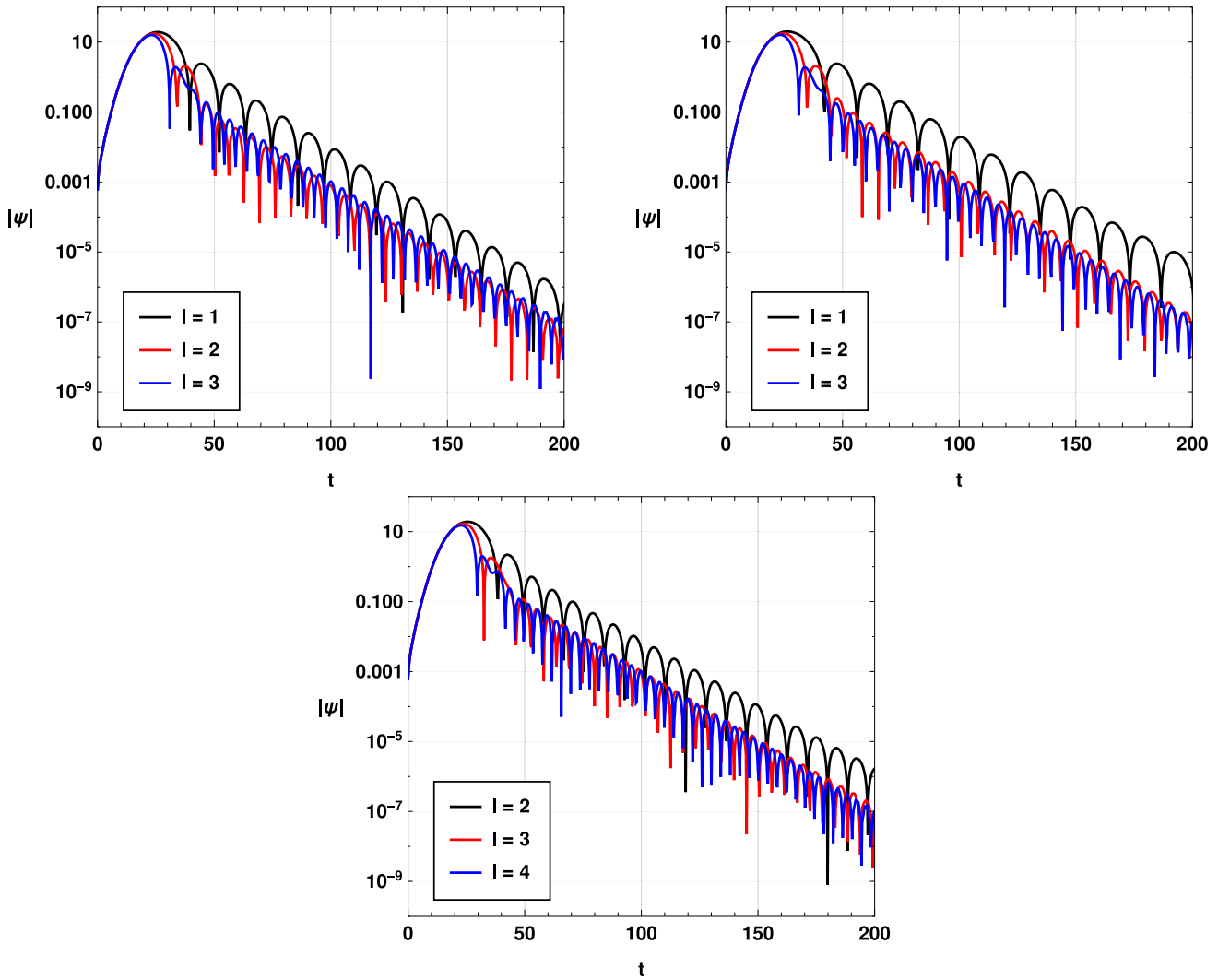

Fig. 7 The time-domain profiles of the massless scalar perturbations (first panel), electromagnetic perturbations (second panel) and gravitational perturbations (third panel) for different multipole moments l with the parameter values $M = 1, G = 1, n = 0, \alpha = 0.9, c_O = 0.4$ and $Q = 0.3$.

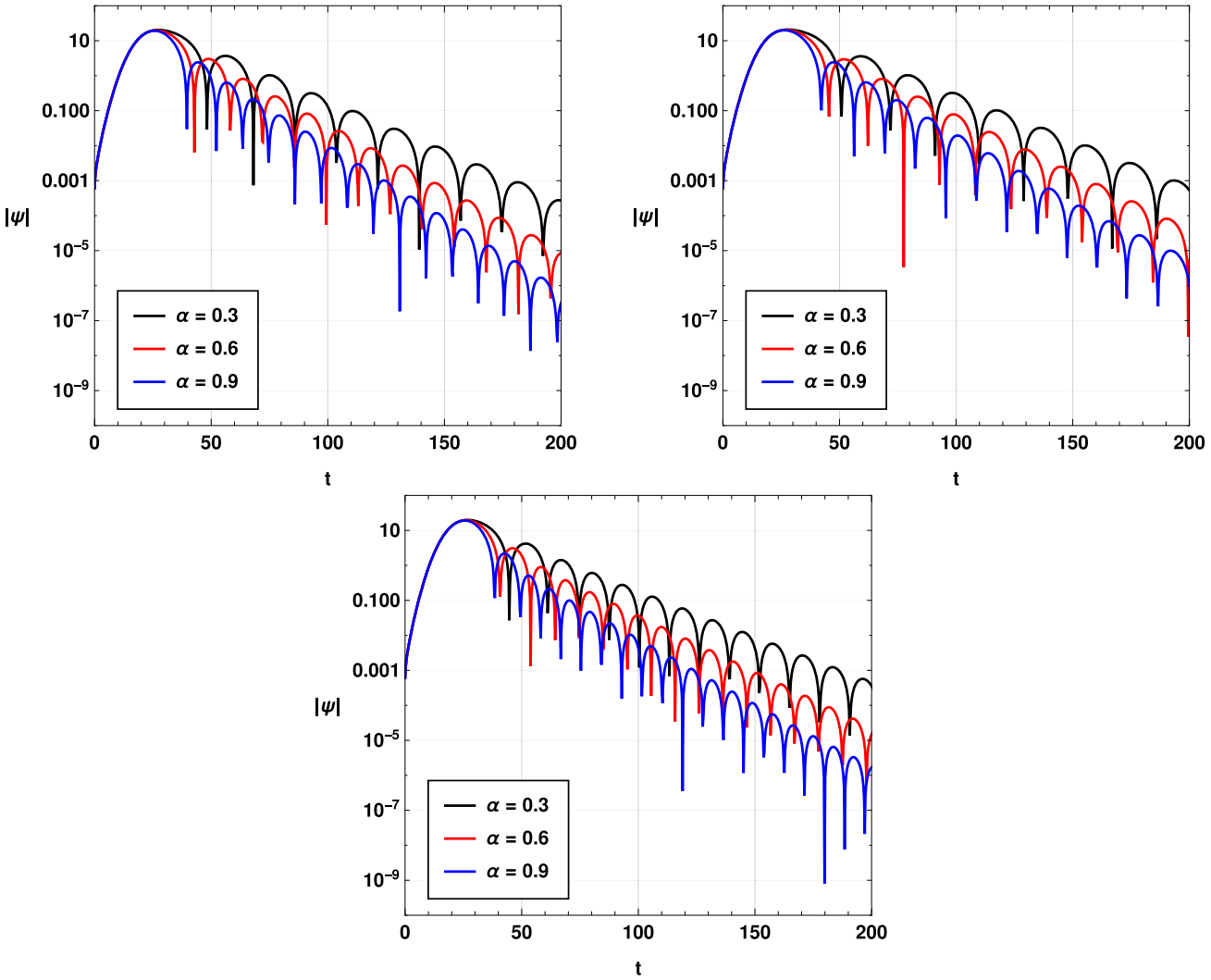

Fig. 8 The time-domain profiles of the massless scalar perturbations (first panel), electromagnetic perturbations (second panel) and gravitational perturbations (third panel) for different values of the model parameter α with the parameter values $M = 1, G = 1, n = 0, c_{\mathrm{O}} = 0.4$ and $Q = 0.3$. For scalar and electromagnetic perturbations, $l = 1$ and for gravitational perturbations $l = 2$

utilizes the advancements suggested by Ref. [159], where Padé approximations are incorporated into the WKB method, yielding more precise results.

Building on these improvements, we apply the Padé-averaged 6th-order WKB approximation technique to estimate the QNMs of black holes. The incorporation of Padé averaging has been shown to enhance the precision of QNM estimates, as demonstrated in prior studies such as Ref. [158]. By using this refined approach, we seek to achieve more accurate and reliable estimates of QNMs, which will be compared with earlier results to validate our findings. This comparative analysis is critical in evaluating the robustness of the WKB method and advancing our understanding of black hole dynamics.

In this subsection, we present QNM values computed using the Padé-averaged 6th-order WKB approximation, along with error estimates in Tables 1, 2 and 3. The 3rd and 4th columns of these tables show the errors associated with the WKB approximation, specifically the root mean square (rms) error, denoted as $\triangle_{rms}$, and the error term Δ_6, defined as [158]

$$\Delta_6 = \frac{|\,\omega_7 - \omega_5\,|}{2}, \tag{36}$$

where ω_7 and ω_5 represent the QNMs computed using the 7th and 5th-order Padé-averaged WKB methods, respectively. By analyzing these errors, we provide a detailed assessment of the accuracy of our QNM estimates, further reinforcing

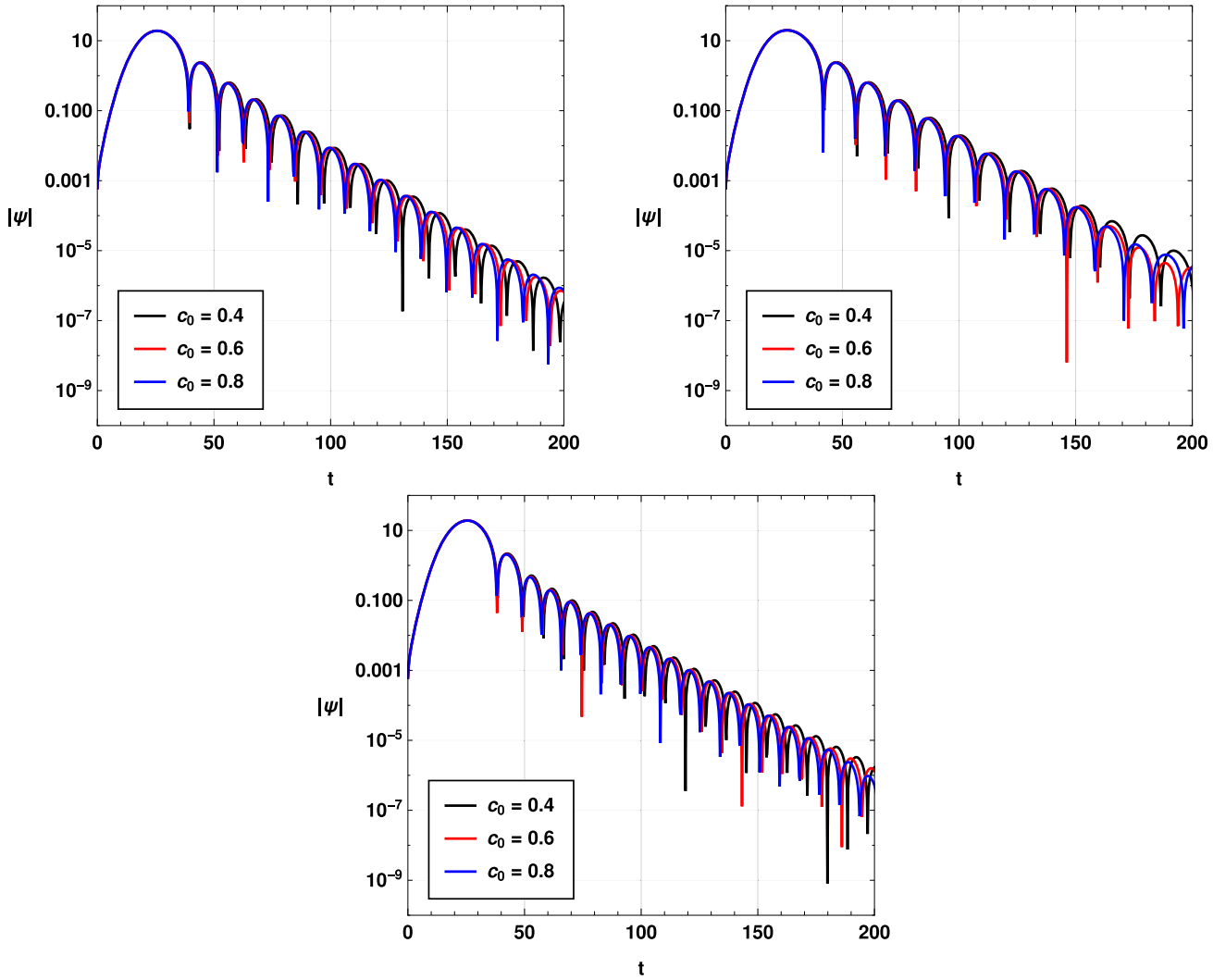

Fig. 9 The time-domain profiles of the massless scalar perturbations (first panel) and electromagnetic perturbations (right panel) for different values of c_O with the parameter values $M = 1, G = 1, n = 0, \alpha = 0.9$ and $Q = 0.3$. For scalar and electromagnetic perturbations, $l = 1$ and for gravitational perturbations $l = 2$

the reliability of the WKB method in black hole perturbation analysis.

In Table 1, the QNMs for massless scalar perturbations of a CSBH are presented, with the following model parameters: $c_O = 0.3$, $Q = 0.5$, $\alpha = 0.9$, $G = M = 1$, and overtone number $n = 0$. The results are obtained using the 6th-order WKB approximation method, averaged with Padé approximants. The table also shows two types of errors: the root mean square (rms) error ($\triangle_{rms}$) and the relative error term Δ_6. It is observed that while the Padé-averaged WKB method tends to have larger relative errors (Δ_6) for lower values of the multipole moment l, the rms error ($\triangle_{rms}$) is relatively smaller. As the multipole moment l increases, both error terms decrease significantly. This behavior is typical of the WKB method, which becomes less accurate when the difference between the multipole moment l and the overtone number n is small. Additionally, the quasinormal frequencies and damping rates increase as the value of l increases. In the last column of this table, we have shown the QNMs obtained from eikonal approximation. One may see that the results obtained using the eikonal approximation deviates significantly for small multipole moments. It is due to the larger errors associated with the method. The Padé averaged 6th order WKB approximation is more accurate than the eikonal approximation, and as seen from the Table, errors associated with the higher order WKB method decrease with an increase in the values of the multiple moment l [158]. Usually, the WKB method is not suitable for $n > l$ as such a scenario results in higher errors. Apart from this, if the potential has more than one peak, the WKB method can not provide reliable results.

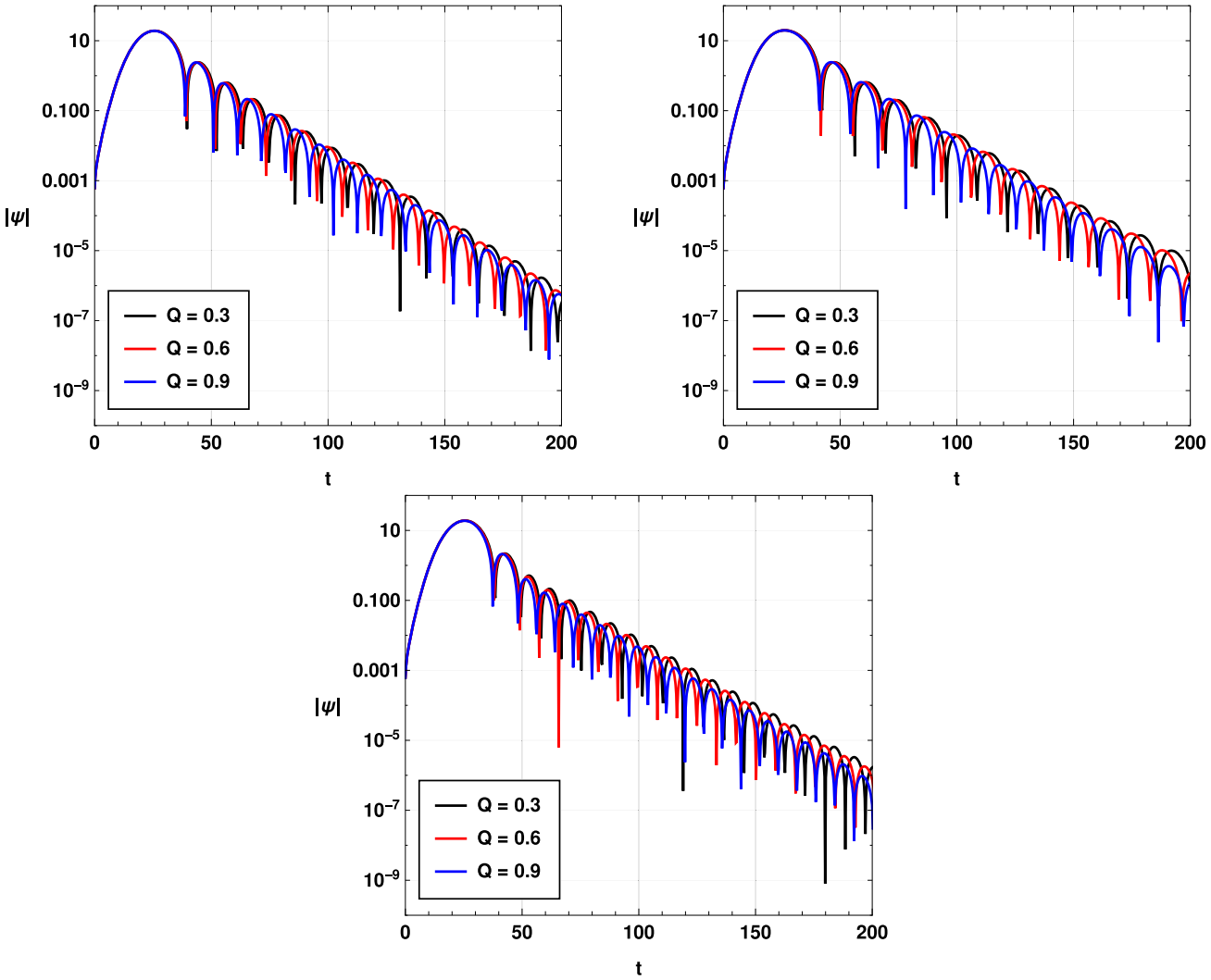

Fig. 10 The time-domain profiles of the massless scalar perturbations (first panel) and electromagnetic perturbations (right panel) for different values of Q with the parameter values $M = 1$, $G = 1$, $n = 0$, $\alpha = 0.9$ and $c_O = 0.4$. For scalar and electromagnetic perturbations, $l = 1$ and for gravitational perturbations $l = 2$

Table 1 The scalar QNMs of the CSBH for $n = 0$, $M = 1$, $G = 1$, $\alpha = 0.9$, $Q = 0.5$ and $c_O = 0.3$ using the 6th order WKB approximation method averaged with Padé approximants

l	Padé averaged WKB	$\triangle_{rms}$	Δ_6	Eikonal
$l = 1$	$0.27937 - 0.094328i$	4.74121×10^{-6}	0.0000176752	$0.313058 - 0.0924115\,i$
$l = 2$	$0.464267 - 0.0924163i$	6.44457×10^{-7}	2.44832×10^{-6}	$0.485099 - 0.0916926\,i$
$l = 3$	$0.649716 - 0.0918554i$	5.0719×10^{-8}	4.46484×10^{-7}	$0.664713 - 0.0914789\,i$
$l = 4$	$0.835258 - 0.0916204i$	8.56836×10^{-9}	1.14886×10^{-7}	$0.846959 - 0.0913906\,i$
$l = 5$	$1.02083 - 0.0915005i$	2.25924×10^{-9}	4.54218×10^{-8}	$1.03042 - 0.0913459\,i$

Table 2 presents the QNMs for electromagnetic perturbations under the same model parameters and method used in Table 1. Similar to the case of scalar perturbations, the errors are larger for lower multipole moments l, but as l increases, both the rms and relative errors decrease. This indicates that the accuracy of the WKB approximation improves with larger multipole moments, consistent with the results observed in scalar perturbations.

In Table 3, we have shown the QNMs for the gravitational perturbation. In this case, one may note that the oscillation

Table 2 The electromagnetic QNMs of the CSBH for $n = 0$, $M = 1$, $G = 1$, $\alpha = 0.9$, $Q = 0.5$ and $c_{\mathrm{O}} = 0.3$ using the 6th order WKB approximation method averaged with Padé approximants

l	Padé averaged WKB	$\triangle_{rms}$	Δ_6	Eikonal
$l = 1$	$0.24098 - 0.0880597i$	3.87696×10^{-6}	0.0000234139	$0.276403 - 0.0866553\,i$
$l = 2$	$0.442189 - 0.090206i$	1.83268×10^{-7}	2.32131×10^{-6}	$0.463342 - 0.0895359\,i$
$l = 3$	$0.634127 - 0.0907312i$	2.44681×10^{-8}	4.26197×10^{-7}	$0.649234 - 0.0903676\,i$
$l = 4$	$0.82319 - 0.090941i$	5.37897×10^{-9}	1.09616×10^{-7}	$0.834941 - 0.0907157\,i$
$l = 5$	$1.01098 - 0.0910459i$	1.60587×10^{-9}	4.17134×10^{-8}	$1.02059 - 0.0908933\,i$

Table 3 The gravitational QNMs of the CSBH for $n = 0$, $M = 1$, $G = 1$, $\alpha = 0.9$, $Q = 0.5$ and $c_{\mathrm{O}} = 0.3$ using the 6th order WKB approximation method averaged with Padé approximants

l	Padé averaged WKB	$\triangle_{rms}$	Δ_6	Eikonal
$l = 2$	$0.360726 - 0.0851828i$	8.72691×10^{-7}	0.0000263476	$0.383891 - 0.084425\,i$
$l = 3$	$0.578576 - 0.0883191i$	1.02995×10^{-10}	8.73876×10^{-8}	$0.594274 - 0.0879164\,i$
$l = 4$	$0.780778 - 0.0895376i$	4.34691×10^{-9}	3.10375×10^{-8}	$0.792796 - 0.0892975\,i$
$l = 5$	$0.976597 - 0.0901268i$	1.49305×10^{-9}	1.19004×10^{-8}	$0.986356 - 0.0899675\,i$

frequency of GWs is comparatively lower in comparison to those found for the cases of scalar and electromagnetic perturbations. The damping or decay rate is also less than that of scalar as well as electromagnetic perturbations.

When comparing the results from these tables, it is clear that the quasinormal frequencies and damping rates for scalar perturbations are the highest and for gravitational perturbations, the lowest for these three types. This difference highlights the impact of the type of perturbation on the black hole's quasinormal modes, where gravitational and electromagnetic perturbations generally produce lower frequency oscillations and slower decay rates compared to massless scalar perturbations. As anticipated, the eikonal estimate deviates noticeably from Padé–WKB at low l (cf. Tables 1, 2, 3), with the discrepancy decreasing monotonically with l and becoming sub-percent for $l \gtrsim 4$.

To explore the effects of the model parameters on the QNM spectrum, we have explicitly plotted the real and imaginary components of the QNMs with respect to these parameters. For this purpose, we employed the Padé-averaged 6th-order WKB approximation method, choosing a higher value of the multipole moment l. The rationale for selecting a larger value of l is that the WKB method's associated error diminishes significantly at higher values of l. In Fig. 11, the variation of real (left) and imaginary (right) QNMs with respect to the model parameter α is shown for scalar perturbations. As α increases, the real QNMs, which correspond to the oscillation frequencies, exhibit a significant increase, following an almost linear pattern. It's important to note that $\alpha < 1$ implies a de Sitter (dS) spacetime, meaning that de Sitter black holes have lower oscillation frequencies compared to anti-de Sitter (AdS) or asymptotically flat black holes. The damping rate or decay rate of GWs also increases linearly with α. The same behavior is observed in Fig. 12 for electromagnetic perturbations and in Fig. 13 for gravitational perturbations. However, in the case of gravitational perturbations, both oscillation frequencies and damping rate are found to be lower than electromagnetic and scalar perturbations.

In Fig. 14, the variation of the ringdown GW frequency and damping rate with respect to the parameter c_{O} is depicted for scalar perturbations. For positive values of c_{O}, both real quasinormal frequencies and damping rates increase non-linearly, with the variation being more pronounced for smaller values of c_{O}. As c_{O} approaches 0.4, the variation in both real and imaginary QNMs becomes negligible. In contrast, for negative values of c_{O}, both the oscillation frequency and damping rate increase non-linearly, reaching a maximum near $c_{\mathrm{O}} = 0$. Notably, a discontinuity in the QNM spectrum is observed at $c_{\mathrm{O}} = 0$. Figures 15 and 16 present similar results for electromagnetic and gravitational perturbations, showing comparable behavior across the parameter space.

The charge parameter Q has a significant and nonlinear impact on the QNM spectrum of black holes. As shown in Figs. 17, 18 and 19, both the oscillation frequency (real part of QNMs) and the damping rate (imaginary part of QNMs) increase as Q increases. This behavior holds true for all the three perturbations i.e., scalar, electromagnetic and gravitational perturbations, although the precise values of the frequencies and decay rates differ depending on the type of perturbation. In the case of electromagnetic perturbations, the oscillation frequencies and damping rates are generally lower than those observed for scalar perturbations. In the case of gravitational perturbations, the oscillation frequencies and damping rates are found to be the lowest. The non-

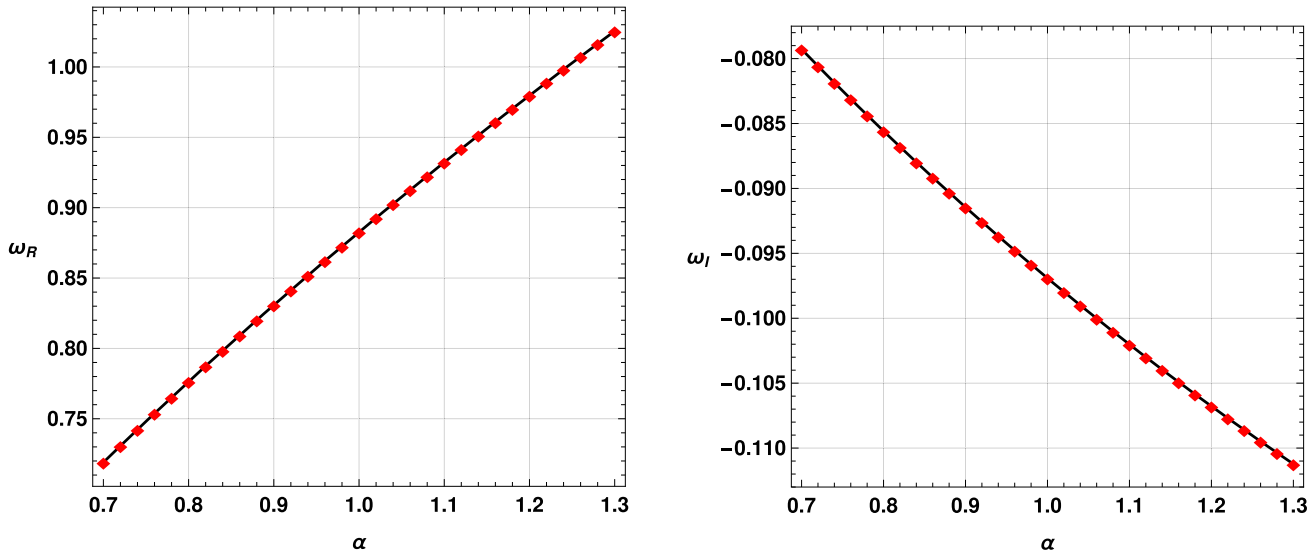

Fig. 11 The real (left panel) and imaginary (right panel) parts of the QNMs of the CSBH for massless scalar perturbations as a function of the vacuum energy parameter α with $M = 1$, $G = 1$, $n = 0$, $l = 4$ and $c_{\mathrm{O}} = 0.4$

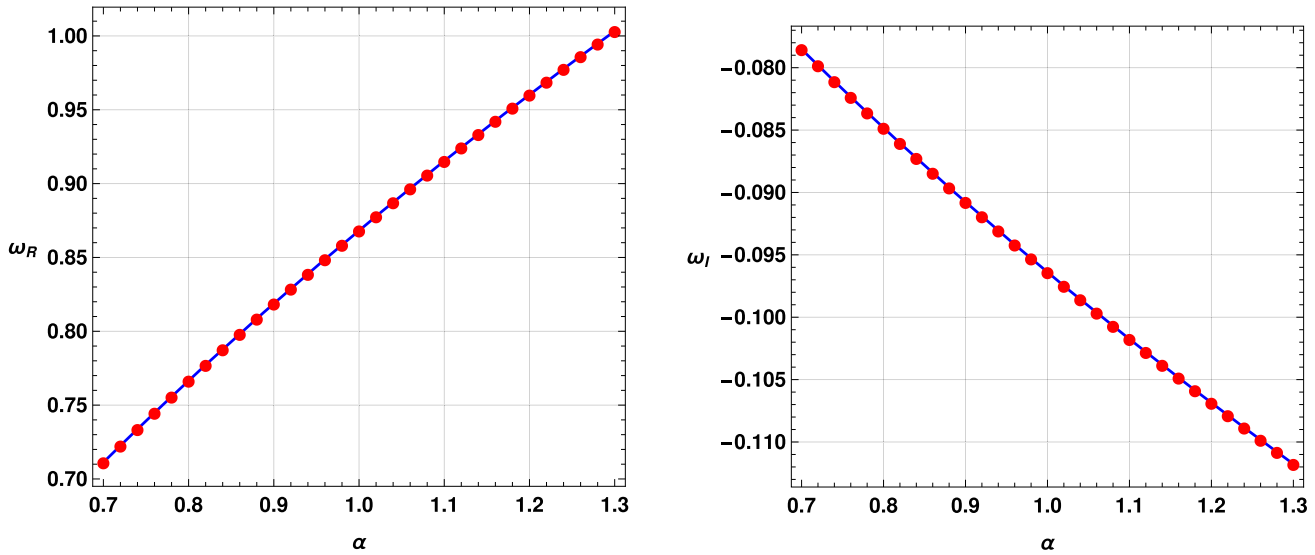

Fig. 12 The real (left panel) and imaginary (right panel) parts of the QNMs of the CSBH for electromagnetic perturbations as a function of the vacuum energy parameter α with $M = 1$, $G = 1$, $n = 0$, $l = 4$ and $c_{\mathrm{O}} = 0.4$

linear nature of the relationship between Q and the QNMs suggests that even small changes in the charge parameter can have a pronounced effect on the behavior of the black hole.

Physically, the increase in oscillation frequency with higher Q can be understood in the context of the black hole's enhanced electric field. As the black hole's charge increases, the strength of its electromagnetic field grows, which leads to more tightly bound perturbations. This results in higher frequency oscillations for perturbing fields around the black hole. Furthermore, the increase in the damping rate with Q indicates that the perturbations decay more rapidly, meaning that the charged black hole tends to settle down faster after being perturbed. The faster decay is likely due to the increased energy stored in the electromagnetic field, which enhances the dissipation of perturbing waves.

The physical significance of these findings is particularly relevant in the context of astrophysical black holes that may possess charge. Although most observed black holes are expected to have negligible charge due to charge-neutralizing effects in astrophysical environments, highly charged black holes are theoretically possible in certain exotic scenarios. For example, primordial black holes formed in the early universe could retain some charge if they formed in environments where neutralizing particles were absent. Understand-

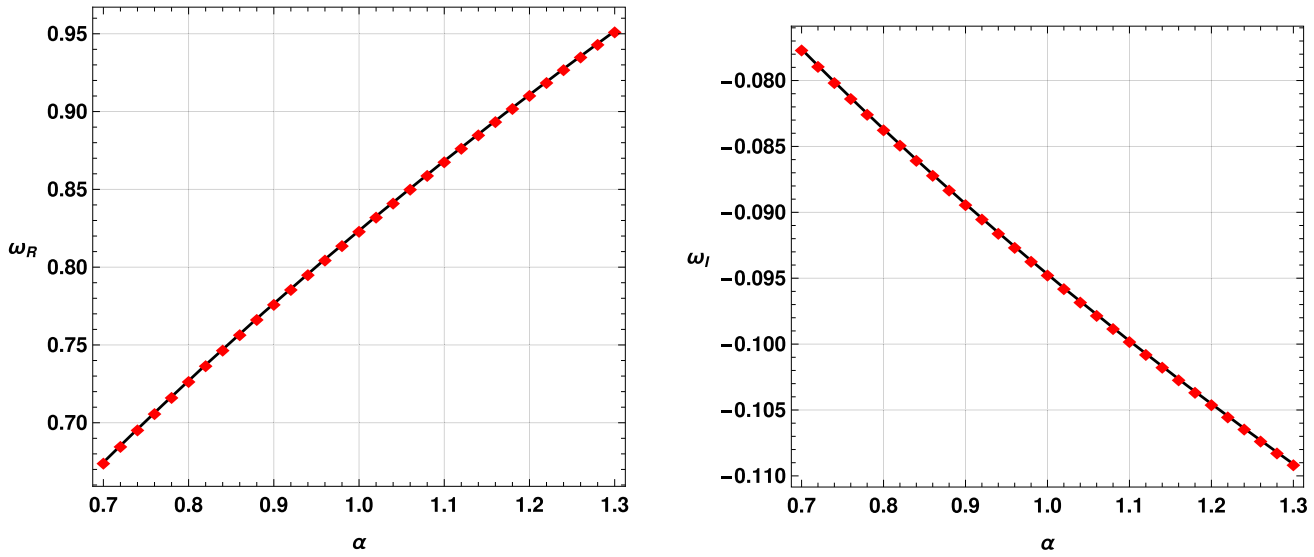

Fig. 13 The real (left panel) and imaginary (right panel) parts of the QNMs of the CSBH for gravitational perturbations as a function of the vacuum energy parameter α with $M = 1$, $G = 1$, $n = 0$, $l = 4$ and $c_{\mathrm{O}} = 0.4$

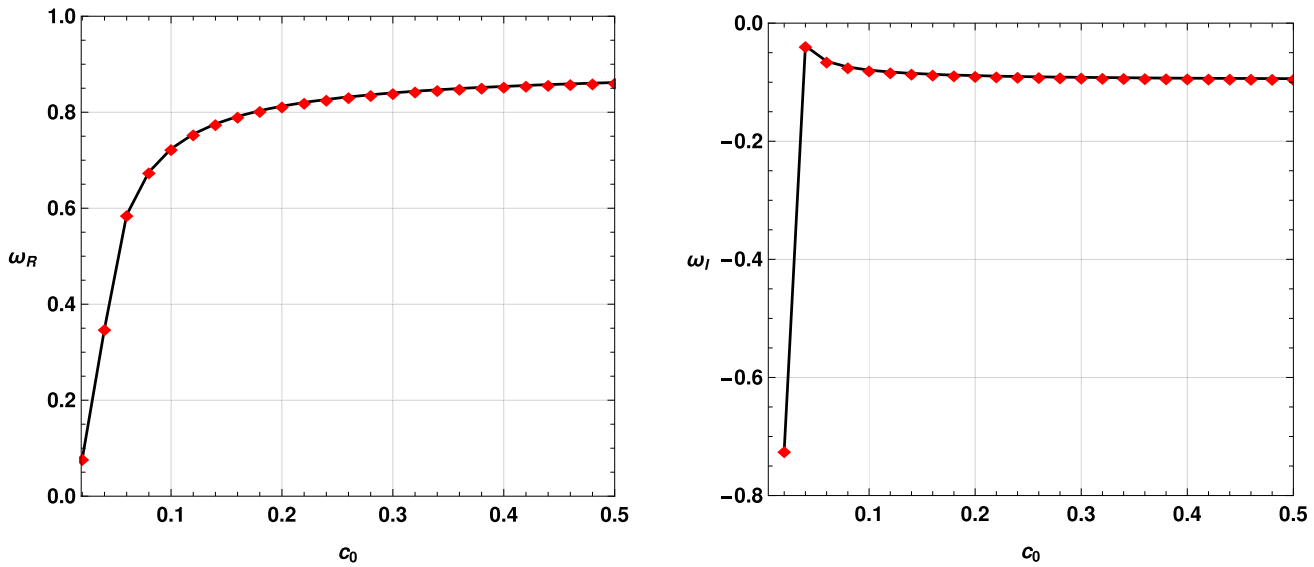

Fig. 14 The real (left panel) and imaginary (right panel) parts of the QNMs of the CSBH for massless scalar perturbations as a function of the symmergent parameter c_{O} with $M = 1$, $G = 1$, $n = 0$, $l = 4$, $Q = 0.55$ and $\alpha = 0.9$

ing the impact of charge on the QNM spectrum is therefore important for detecting or constraining the properties of such exotic black holes through gravitational wave observations.

These results highlight that the CSBH model exhibits behavior distinct from other well-known charged black hole solutions, such as the Reissner–Nordström black hole. In addition, the impact of the symmergent parameters on the QNM spectrum is distinct from that of the black hole's charge, further emphasizing the uniqueness of this model. The study of QNMs in charged black holes, and their dependence on parameters such as Q, continues to be an important area of research for both theoretical and observational astrophysics [53,95,98,99,104–109]. Gravitational-wave observations have been used to constrain the possible electric charge of black hole remnants. Analyses of LIGO/Virgo events found no evidence for nonzero charge, but placed loose bounds on the charge-to-mass ratio, $Q/M \lesssim 0.3$–0.5 [110]. Numerical relativity simulations further showed that the inspiral phase is more sensitive to charge than the ringdown, with GW150914 data still compatible with moderate charges [111]. Even tiny charges, at the level of $Q/M \sim 10^{-4}$, could in principle power electromagnetic counterparts to mergers [112], although no such signals have been confirmed. Extensions to Kerr–Newman black holes demonstrate that charge

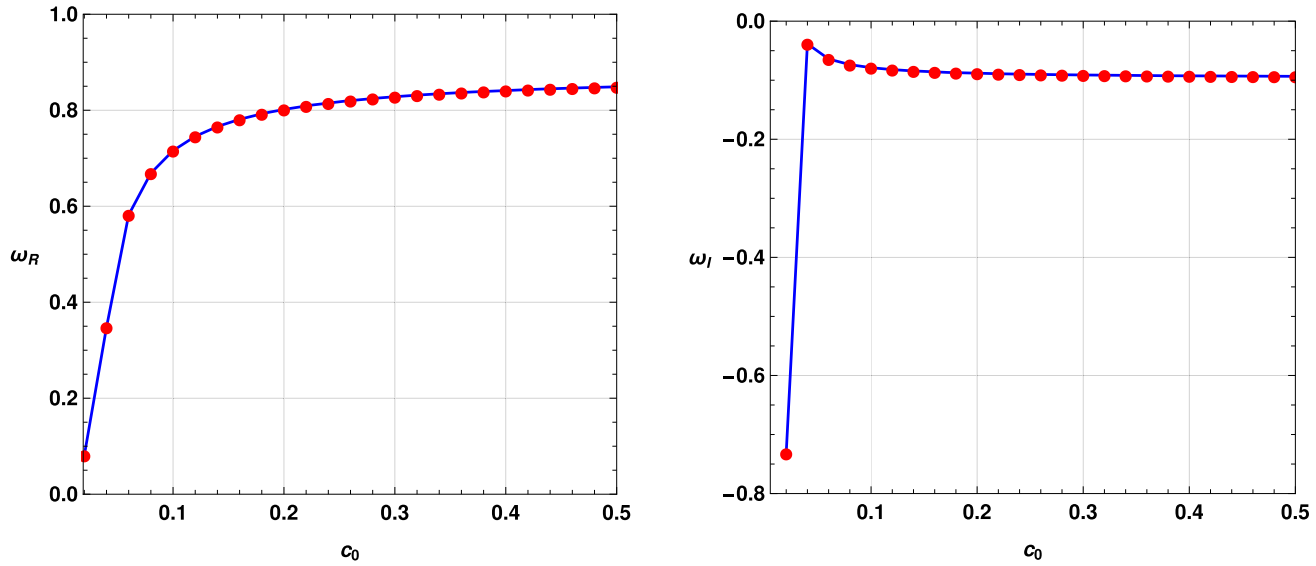

Fig. 15 The real (left panel) and imaginary (right panel) parts of the QNMs of the CSBH for electromagnetic perturbations as a function of the symmergent parameter c_0 with $M = 1$, $G = 1$, $n = 0, l = 4$, $Q = 0.55$ and $\alpha = 0.9$.

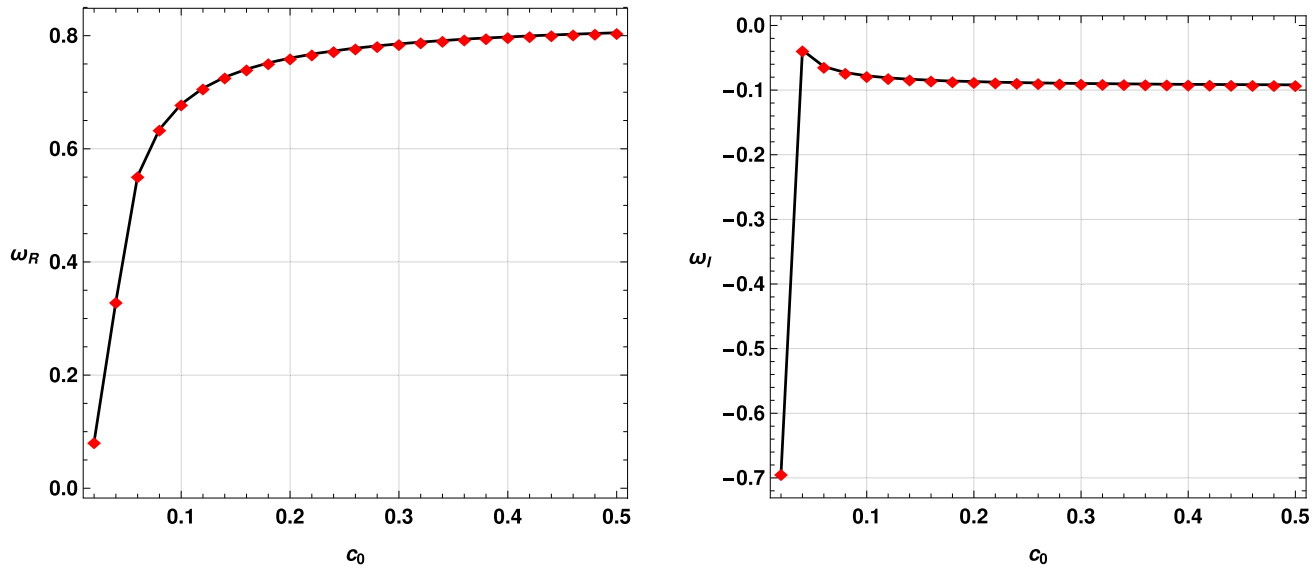

Fig. 16 The real (left panel) and imaginary (right panel) parts of the QNMs of the CSBH for gravitational perturbations as a function of the symmergent parameter c_0 with $M = 1$, $G = 1$, $n = 0, l = 4$, $Q = 0.55$ and $\alpha = 0.9$

primarily perturbs QNM frequencies in a perturbative way [113,114]. Future detectors such as LISA may allow high-precision spectroscopy to either detect or place tighter bounds on charge.

These findings also differ from results obtained for wormhole configurations, as studied in [128,129], demonstrating that the symmergent model's predictions for QNMs are distinct even when compared to other exotic spacetime geometries. This underscores the importance of QNMs as a tool for probing the underlying nature of black holes and the influence of additional parameters such as charge and symmergent contributions on their dynamical properties.

3.7 Validity of Hod's conjecture

In the study of black hole physics, a key question concerns how fundamental properties such as mass, charge, and angular momentum are reflected in a black hole's quasinormal modes. In the previous part of our investigation, we have investigated how the model parameters associated with the black hole spacetime impacts the QNMs spectrum. Now, in

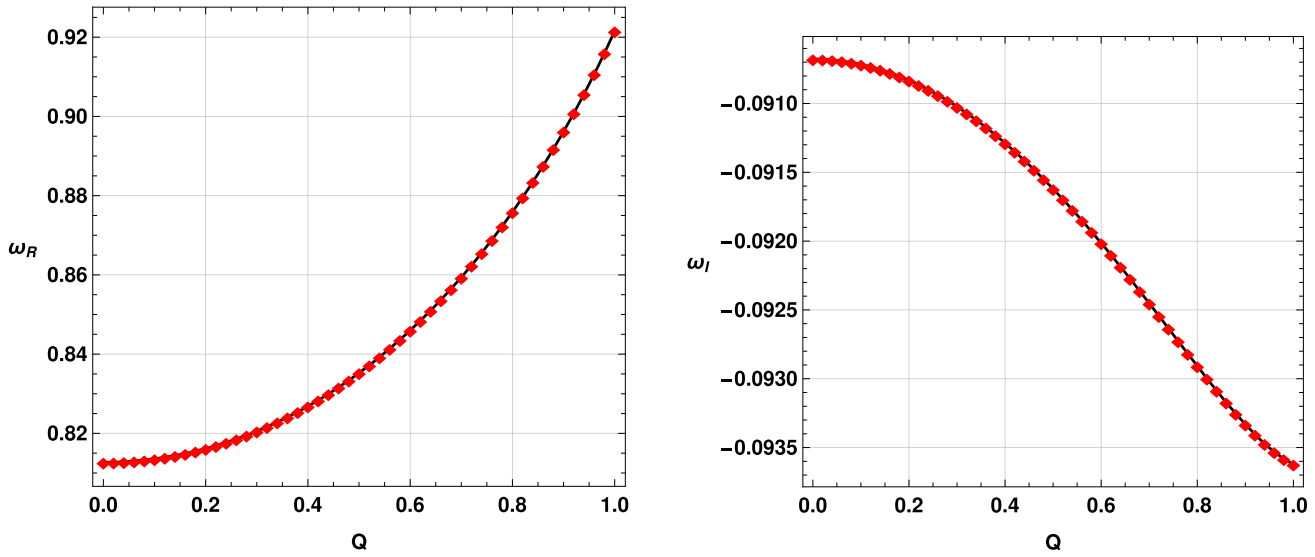

Fig. 17 The real (left panel) and imaginary (right panel) parts of the QNMs of the CSBH for massless scalar perturbations as a function of the charge parameter Q with $M = 1$, $G = 1$, $n = 0$, $l = 4$, $\alpha = 0.9$ and $c_{\rm O} = 0.3$

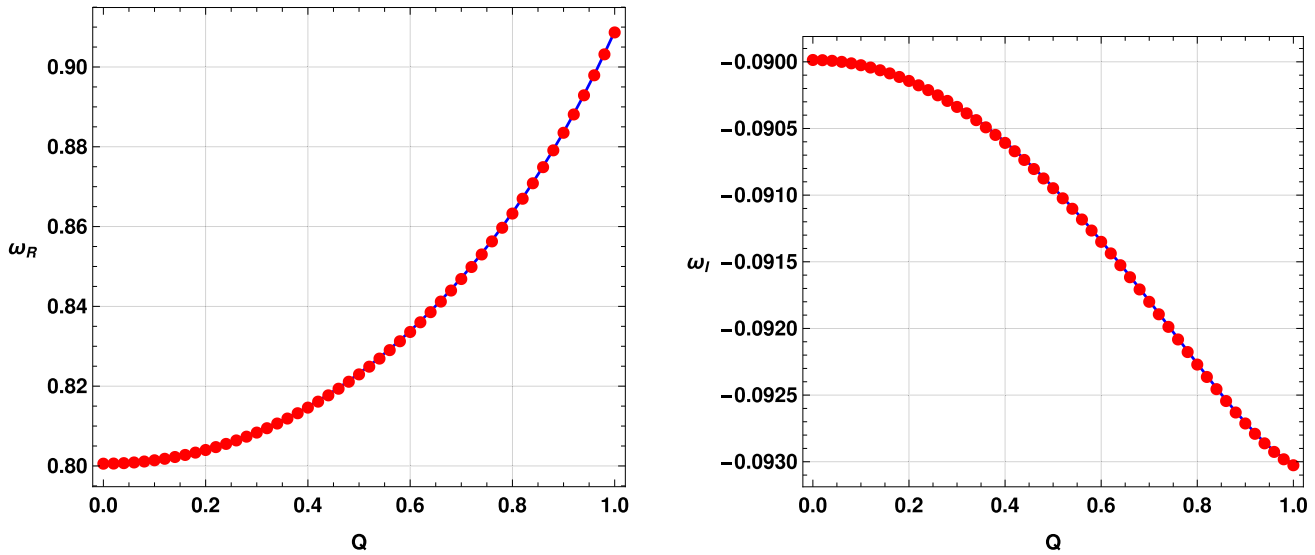

Fig. 18 The real (left panel) and imaginary (right panel) parts of the QNMs of the CSBH for electromagnetic perturbations as a function of the charge parameter Q with $M = 1$, $G = 1$, $n = 0$, $l = 4$, $\alpha = 0.9$ and $c_{\rm O} = 0.3$.

this subsection, we investigate the validity of Hod's conjecture for the black hole spacetime. In a seminal work, Ref. [130], Hod proposed a universal constraint on the quasinormal mode spectrum of any black hole. Specifically, he conjectured that there always exists a frequency ω in the spectrum such that the imaginary part of ω satisfies the following bound:

$$|\Im(\omega)| \leq \pi T_H, \tag{37}$$

where T_H denotes the Hawking temperature of the black hole. For any static, spherically symmetric black hole the Hawking temperature is related *directly* to the surface gravity κ_H at the event horizon r_h via $T_H = \frac{\kappa_H}{2\pi}$, $\kappa_H = \frac{1}{2} h'(r)\big|_{r=r_h}$, [137,169]. Using our metric function $h(r)$, we obtain

$$T_H = \frac{1}{4\pi}\left[\frac{2GM}{r_h^2} - \frac{Q^2}{\alpha\, r_h^3} - \frac{(1-\alpha)}{12\pi G c_{\rm O}}\, r_h\right], \tag{38}$$

which reduces to the standard limits: (i) Schwarzschild $T_H = 1/(4\pi r_h)$ for $Q \to 0$ and $(1-\alpha)/c_{\rm O} \to 0$ with $r_h = 2GM$; (ii) Reissner–Nordström with the identification $\hat{Q}^2 = Q^2/(2\alpha)$ and vanishing cosmological term. With M expressed through the horizon condition $f(r_h) = 0$, the Hawking temperature reads

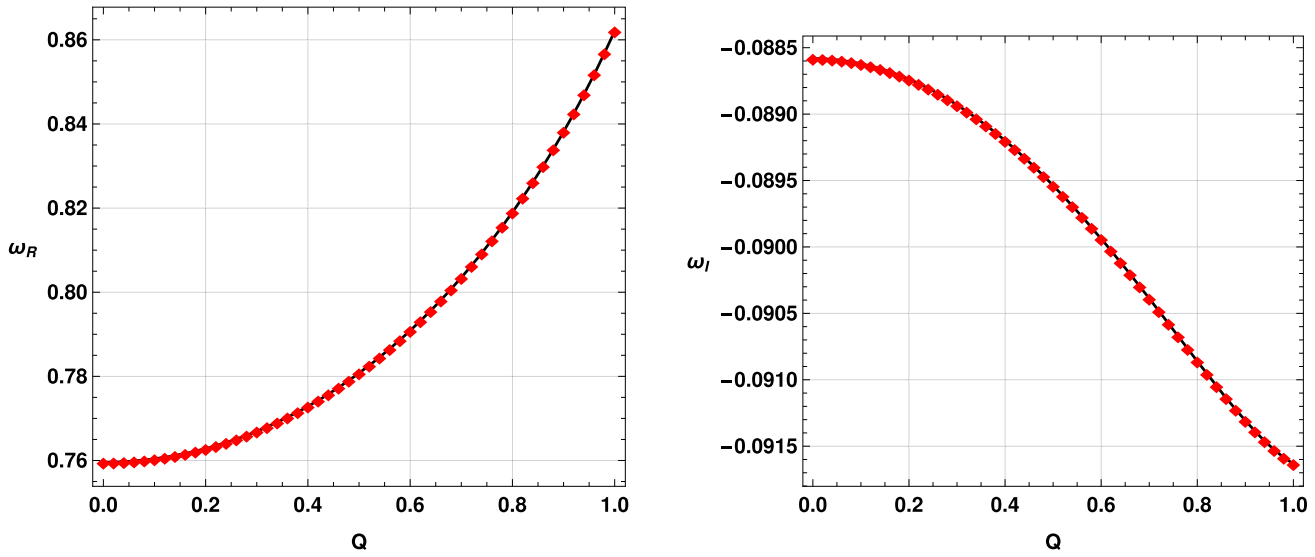

Fig. 19 The real (left panel) and imaginary (right panel) parts of the QNMs of the CSBH for gravitational perturbations as a function of the charge parameter Q with $M = 1$, $G = 1$, $n = 0$, $l = 4$, $\alpha = 0.9$ and $c_{\mathrm{O}} = 0.3$

$$T_H = \frac{1}{4\pi}\left[\frac{1}{r_h} - \frac{Q^2}{2\alpha r_h^3} + \frac{\alpha - 1}{8\pi G c_O}\, r_h\right]. \tag{39}$$

This expression provides a precise relation between the black hole's geometry and its thermodynamic properties. Remarkably, Hod's conjecture is highly general, applying not only to four-dimensional black holes but also to higher-dimensional cases and asymptotically AdS black holes [103,131–133]. Hod's conjecture, as encapsulated in Eq. (37), imposes a significant constraint on the damping rates of quasinormal modes, with the Hawking temperature serving as the critical factor determining the upper bound on the imaginary part of the frequency. This universal bound has profound implications for understanding the stability and oscillatory behaviour of black holes across diverse geometries. Extensive studies have tested the validity of Hod's conjecture across a variety of black hole configurations [134–136]. These investigations have consistently confirmed the conjecture's robustness, establishing it as a cornerstone in the analysis of quasinormal modes and black hole physics.

Here we have graphically visualised the validity of Hod's conjecture in Fig. 20. We see that the Hod's conjecture is valid for the black hole in most of the parameter spaces except for very small values of the parameter c_O. When c_O becomes very small, $|\omega_I|$ increases drastically, violating Hod's conjecture. When c_{O} is very small, the effective cosmological term $\Lambda_{\mathrm{eff}} = (1 - \alpha)/(8\pi G c_{\mathrm{O}})$ becomes large in magnitude, pushing the geometry towards (near-)Nariai configurations with closely spaced horizons. In this near-extremal regime $T_H \to 0$ while the Padé–WKB estimate of $|\Im\omega|$ is known to be less reliable due to the broad, flattened barrier and multiple turning points. Time-domain integrations (and higher-order WKB where convergent) confirm that within the horizon-existence window the Hod bound remains satisfied; the apparent "violations" occur for parameter choices arbitrarily close to the extremal limit where the semi-analytic approximation overestimates damping.

4 Greybody factors

The concept of greybody factors originates from Hawking's groundbreaking discovery in 1975, which demonstrated that black holes are not completely black but emit radiation, now known as Hawking radiation [137]. This emission occurs near the black hole's horizon, but the radiation that reaches a distant observer is altered by a redshift factor, resulting in a modification of its spectrum. This distortion is known as the greybody factor, and it reflects the difference between the initial Hawking radiation and what an observer at infinity detects [138,139]. Various methods have been developed to calculate greybody factors, including significant contributions by Maldacena et al. [140], Fernando [141], and others [93,95,96,116,128,142–147].

4.1 Using the WKB approach

In subsection, we utilize the higher-order WKB approximation method to calculate greybody factors for all the three types of perturbations. This method is especially suited to calculating the reflection and transmission coefficients associated with wave scattering near a black hole. Specifically,

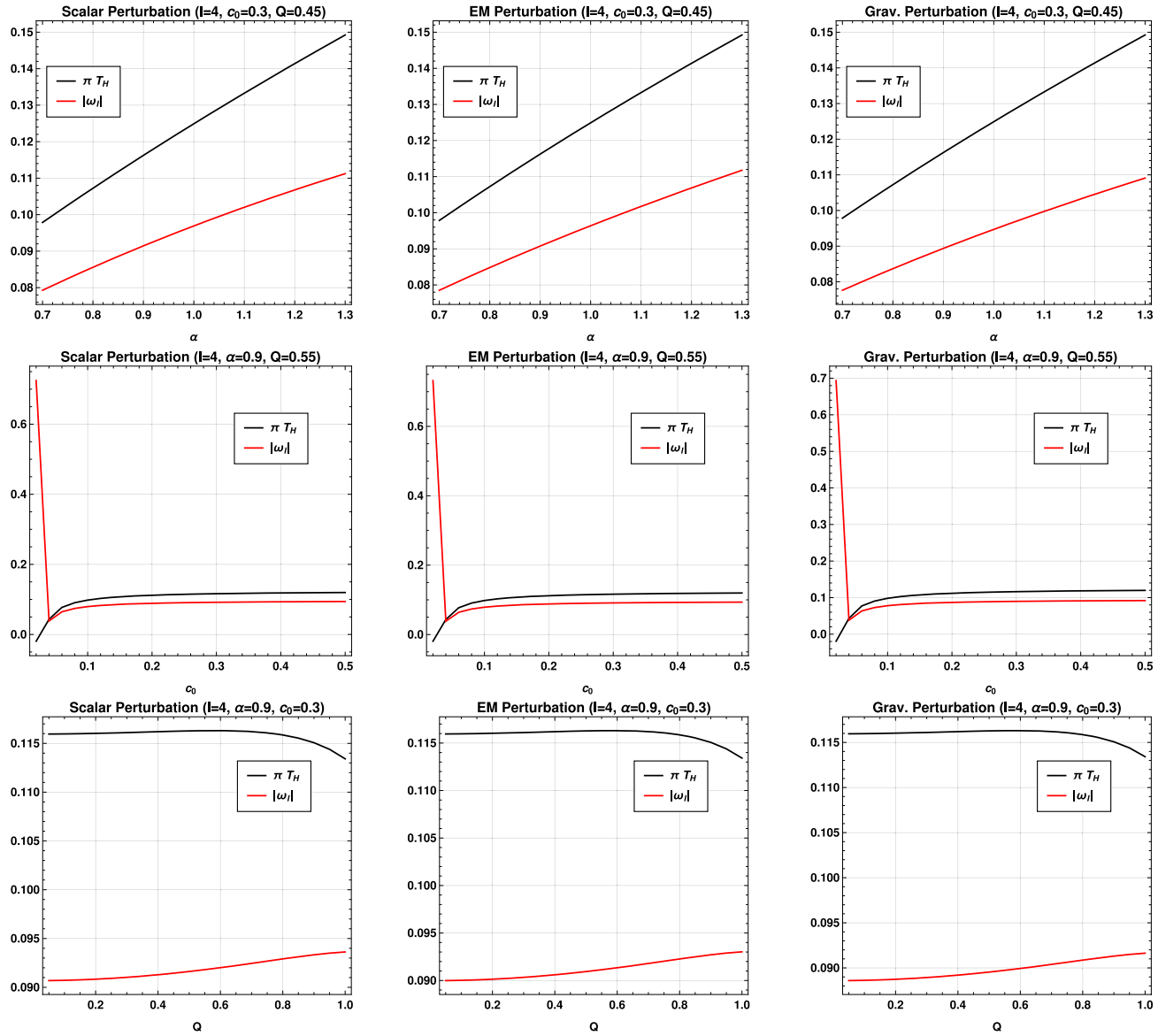

Fig. 20 Graphical visualisation of the validity of Hod's conjecture

we explore the wave equation under boundary conditions that allow for incoming waves from infinity, a scenario analogous to scattering waves from the black hole's horizon. This allows us to determine how much of the incident wave is reflected back versus transmitted across the potential barrier. The transmission coefficient, in this context, is defined as the greybody factor.

The boundary conditions governing the scattering process are expressed as:

$$\Psi = e^{-i\omega r_*} + Re^{i\omega r_*} \quad \text{as} \quad r_* \to +\infty, \quad \Psi = Te^{-i\omega r_*} \quad \text{as} \quad r_* \to -\infty, \tag{40}$$

where R and T represent the reflection and transmission coefficients, respectively. These coefficients satisfy the conservation relation $|T|^2+|R|^2 = 1$, implying that the reflection and transmission probabilities must sum to one. The transmission coefficient $|T|^2$, also known as the greybody factor A, quantifies the fraction of radiation that escapes the potential barrier and reaches an observer at infinity:

$$|A|^2 = 1 - |R|^2 = |T|^2. \tag{41}$$

The WKB approximation provides a means to calculate the reflection coefficient R through the following expression:

$$R = \left(1 + e^{-2i\pi K}\right)^{-\frac{1}{2}}, \tag{42}$$

where the phase factor K is determined by the following equation:

$$K - i\frac{(\omega^2 - V_0)}{\sqrt{-2V_0''}} - \sum_{i=2}^{i=6} \Lambda_i(K) = 0. \tag{43}$$

which involves the maximum value of the effective potential V_0, its second derivative V_0'', and higher-order corrections Λ_i, extending up to the 6th order [156–159]. The WKB method, while effective, is less accurate at low frequencies where reflection tends to be total, causing the greybody factors to approach zero. Nevertheless, this does not substantially affect the calculation of energy emission rates.

Given the robustness and broad applicability of the WKB method in various contexts, including the study of black hole perturbations and greybody factors, a detailed review is beyond the scope of this paper. For more in-depth discussions, we refer readers to comprehensive reviews in the literature [51,161].

The figures presented in Figs. 21, 22, 23, 24 and 25 provide a detailed analysis of the behavior of the greybody factors for massless scalar, electromagnetic and gravitational perturbations under varying model parameters. Each figure highlights how different parameters influence the absorption probabilities, offering valuable insights into black hole dynamics in the context of symmergent gravity.

In Fig. 21, we observe the variation of greybody factors $|A_s|^2$ for scalar perturbations (first panel), $|A_e|^2$ for electromagnetic perturbations (second panel) and $|A_g|^2$ for gravitational perturbations (third panel) as the multipole moment l changes. As the multipole moment increases, the peak of the greybody factors shifts to higher frequencies (ω), indicating that higher-energy modes are more strongly excited at larger l values. Interestingly, gravitational perturbations reach their maximum absorption at slightly lower frequencies compared to scalar and electromagnetic perturbations. This suggests that gravitational waves interact more efficiently at lower frequencies, leading to earlier peaks in absorption than scalar and electromagnetic waves for the same multipole moments.

In Fig. 22, the effects of the model parameter α on the greybody factors are examined. The greybody factors for all the three perturbations exhibit a noticeable decrease as α increases. This implies that black holes with smaller α values have higher absorption and scattering probabilities, effectively capturing more incoming radiation or particles. As α increases, the greybody factors drop, indicating that black holes become less interactive with the surrounding radiation and allow more of it to escape. The sensitivity of the greybody factors to α underscores the significance of this parameter in controlling the interaction between black holes and external perturbations.

A similar pattern emerges in Fig. 23, which explores the impact of the model parameter $c_{\rm O}$ on the greybody factors. All the three perturbations display higher greybody factors for smaller values of $c_{\rm O}$, with a clear decrease as $c_{\rm O}$ increases. This suggests that black holes with lower values of $c_{\rm O}$ are more effective at absorbing radiation, while higher values of $c_{\rm O}$ reduce this efficiency. The sensitivity of the greybody factors to $c_{\rm O}$ diminishes at higher values, indicating that changes in $c_{\rm O}$ have less impact on black hole absorption in this regime.

Finally, Fig. 25 illustrates the influence of the charge parameter Q on the greybody factors. As the charge Q increases, the greybody factors gradually decrease for all the three types of perturbations. This implies that charged black holes are less efficient at absorbing radiation compared to their neutral counterparts. The decrease in absorption with increasing charge suggests that the presence of charge reduces the interaction between the black hole and incoming waves or particles, leading to lower absorption probabilities.

In summary, these figures reveal that the parameters l, α, $c_{\rm O}$, and Q significantly influence the greybody factors for scalar, electromagnetic and gravitational perturbations. Smaller values of α, $c_{\rm O}$, and Q correspond to higher absorption probabilities, while higher values lead to decreased interaction with incoming radiation. Additionally, gravitational and electromagnetic perturbations tend to reach their maximum absorption at lower frequencies compared to scalar perturbations. These findings enhance our understanding of the intricate dynamics between black holes and external perturbations within the framework of symmergent gravity.

4.2 Rigorous bounds on greybody factors

In this part of our investigation, we consider rigorous bounds on greybody factors by utilizing a different method. Since this portion of the analysis reveals similar behavior between scalar, electromagnetic and gravitational perturbations in terms of greybody factors, we focus on scalar perturbations only for the remainder of the study.

The method we employ is based on the elegant analytical approach originally introduced by Visser (1998) [162], which was subsequently developed further by Boonserm and Visser (2008) [163]. This technique has been widely applied in various contexts, as explored by numerous researchers, including Boonserm et al. (2017, 2019) [164,172], Yang et al. (2022) [170], Gray et al. (2015) [165], Ngampitipan et al. (2012) [166], and others [167,168,170,171]. These studies have demonstrated the robustness of this approach in determining greybody factor bounds across different gravitational systems.

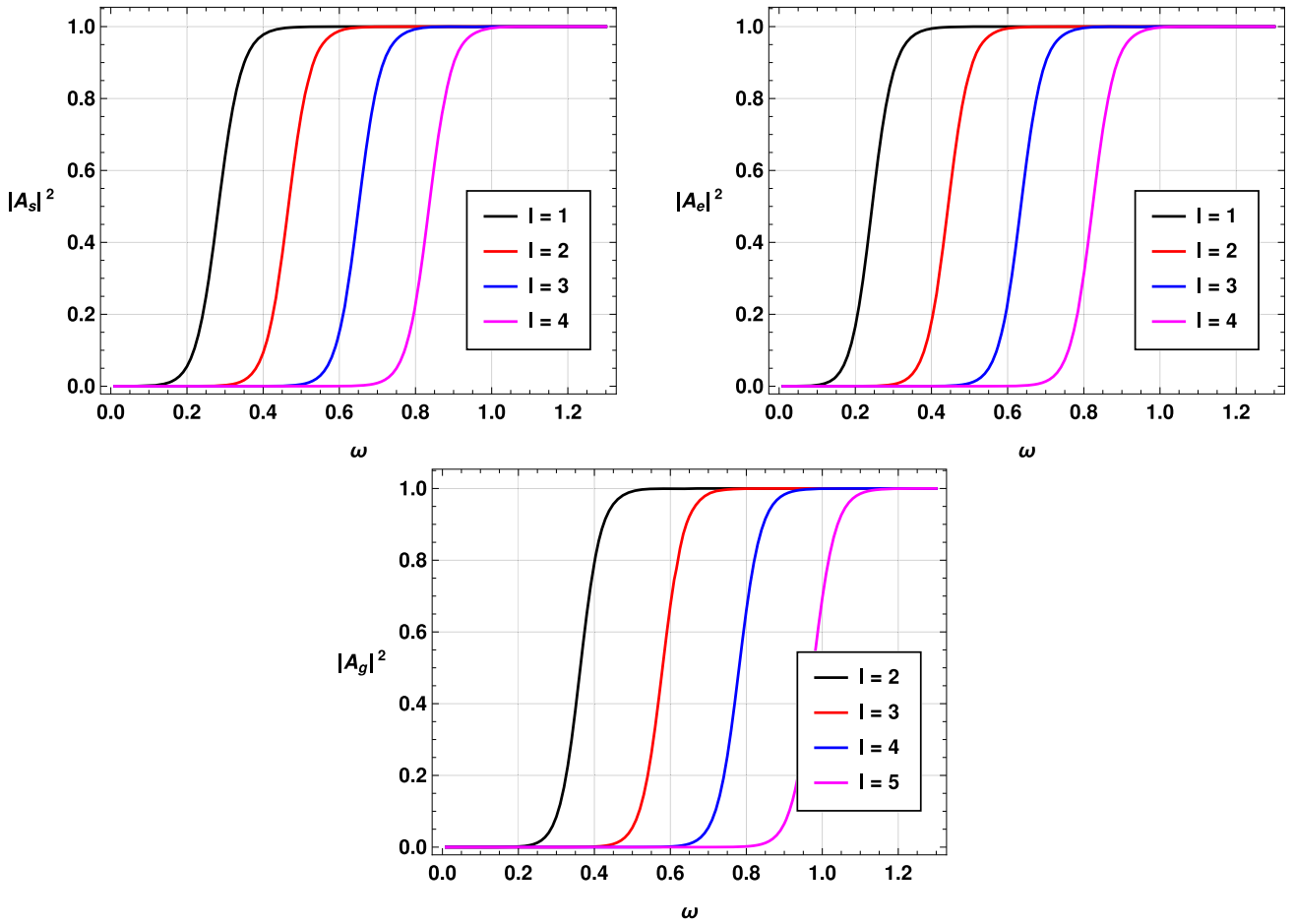

Fig. 21 The greybody factors for massless scalar (first panel), electromagnetic (second panel) and gravitational (third panel) perturbations for different values of the multipole moment l with the parameter values $M = 1$, $G = 1$, $\alpha = 0.9$, $Q = 0.3$ and $c_{\mathrm{O}} = 0.4$

For our analysis, we concentrate specifically on deriving the bounds for the greybody factors of CSBHs. We begin by analyzing the Klein–Gordon equation for the massless scalar field, as discussed in the previous sections, and then reduce the effective potential to the form:

$$V(r) = \frac{l(l+1)h(r)}{r^2} + \frac{h(r)h'(r)}{r}, \tag{44}$$

where $h(r)$ represents the metric function and l is the multipole moment. This potential governs the dynamics of scalar field perturbations in the black hole background.

Using this effective potential, we proceed to derive the rigorous lower bound for the greybody factors, following the methodology laid out by Visser (1998) [162] and Boonserm and Visser (2008) [163]. The bound for the transmission coefficient, denoted as T_b, is given by:

$$T_b \geq \mathrm{sech}^2\left(\frac{1}{2\omega}\int_{-\infty}^{\infty}|V|\,\frac{dr}{h(r)}\right), \tag{45}$$

where ω is the frequency of the perturbation. Here, T_b represents the transmission coefficient, which corresponds to the greybody factor.

To account for the presence of the cosmological constant and the symmergent gravity parameters, we modify the boundary conditions in accordance with the work by Boonserm et al. (2019) [172]. The modified bound is expressed as:

$$A \geq T_b = \mathrm{sech}^2\left(\frac{1}{2\omega}\int_{r_H}^{R_H}\frac{|V|}{h(r)}dr\right) = \mathrm{sech}^2\left(\frac{A_l}{2\omega}\right), \tag{46}$$

where the integral term A_l is defined as:

$$A_l = \int_{r_H}^{R_H}\frac{|V|}{h(r)}dr = \int_{r_H}^{R_H}\left|\frac{l(l+1)}{r^2} + \frac{h'}{r}\right|dr. \tag{47}$$

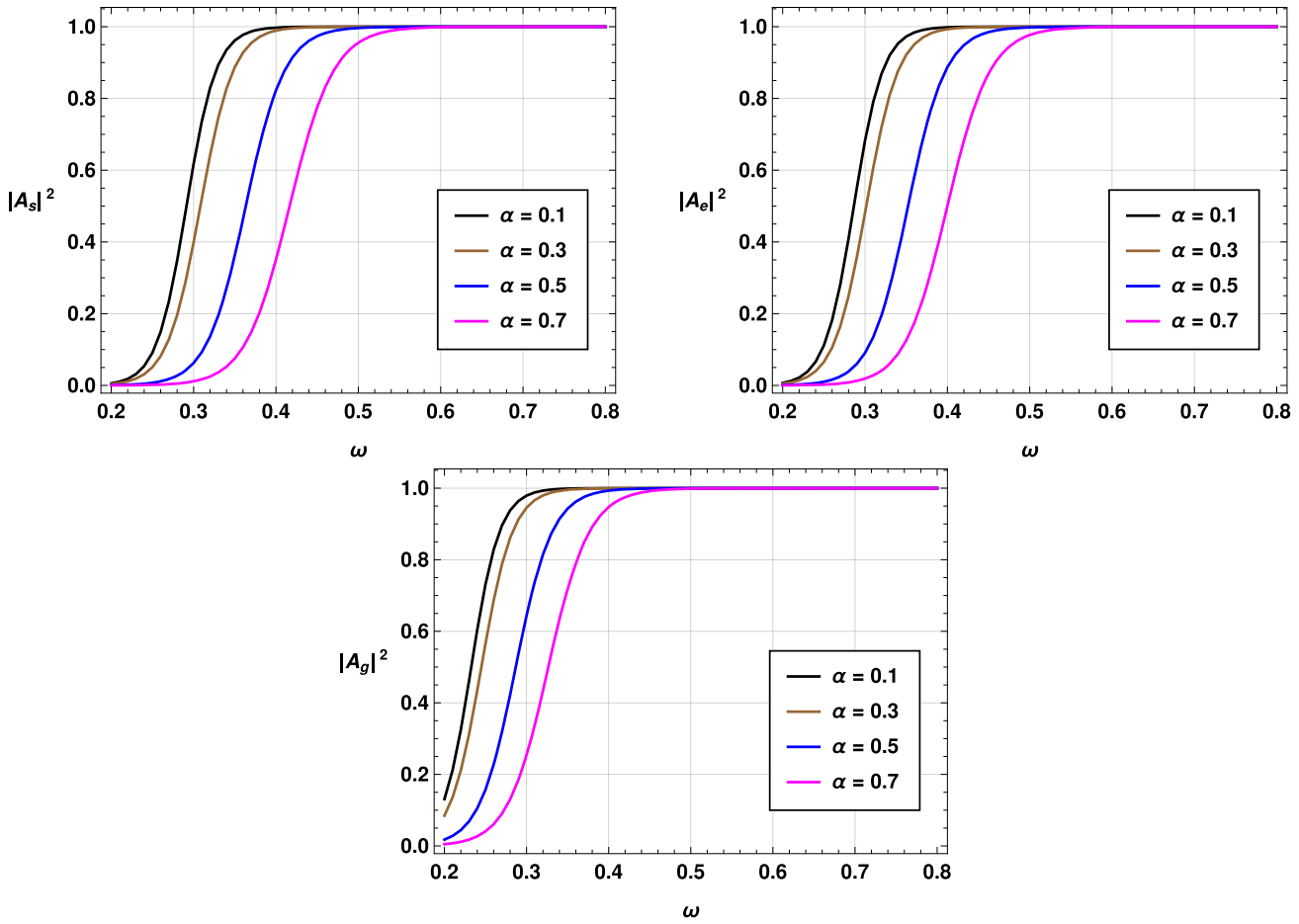

Fig. 22 The greybody factors for massless scalar (first panel), electromagnetic (second panel) and gravitational (third panel) perturbations for different values of the vacuum energy parameter α with the parameter values $M = 1$, $G = 1$, $l = 2$, $Q = 0.3$ and $c_{\mathrm{O}} = 0.4$

In these equations, r_H and R_H denote the event and cosmological horizon radii of the black hole, and the effective potential $V(r)$ is integrated between these radii.

We have successfully computed the rigorous bounds on greybody factors for CSBHs. The formula obtained is expressed as:

$$T_b = \mathrm{sech}^2\left(\frac{(R_H - r_H)\left(4\pi c_{\mathrm{O}} G\left(3\alpha r_H R_H\left(GM\left(r_H + R_H\right) + l(l+1) r_H R_H\right) - Q^2 C_1\right) + (\alpha - 1)\alpha r_H^3 R_H^3\right)}{24\omega\pi\alpha c_{\mathrm{O}} G r_H^3 R_H^3}\right) \tag{48}$$

where $C_1 = \left(r_H R_H + r_H^2 + R_H^2\right)$ and the parameters c_{O}, α, and Q represent the quadratic curvature coupling parameter, the vacuum energy parameter, and the charge of the black hole, respectively.

This expression provides a rigorous lower bound on the greybody factors as a function of various parameters. Our findings demonstrate that the greybody factor bound is sensitive to both the black hole charge and the parameters governing the symmergent gravity model. These results will contribute to a deeper understanding of black hole radiation and the role of symmergent gravity in shaping the interaction between black holes and perturbations.

We compute the transmission coefficient $|A_l(\omega)|^2 = 1 - |R|^2$ using the 6th-order Padé–WKB approach [156–159]. Since the method depends only on the peak V_0 and its derivatives at the turning point, setting $Q \to 0$ and $(1-\alpha)/c_{\mathrm{O}} \to 0$ maps $V_s \to (1 - 2GM/r)\left[\frac{l(l+1)}{r^2} + \frac{2GM}{r^3}\right]$, and our $|A_l|^2$ reduces exactly to the Schwarzschild result (same peak data), as expected.

By performing numerical calculations, we can evaluate the bound and visualize it in Fig. 25 for the case of different l values (on the left panel) and different α values (on the right panel), and in Fig. 26 for the case of different c_{O} values (on the left panel) and different Q values (on the right panel). The resulting graphs indicate that with an increase in the

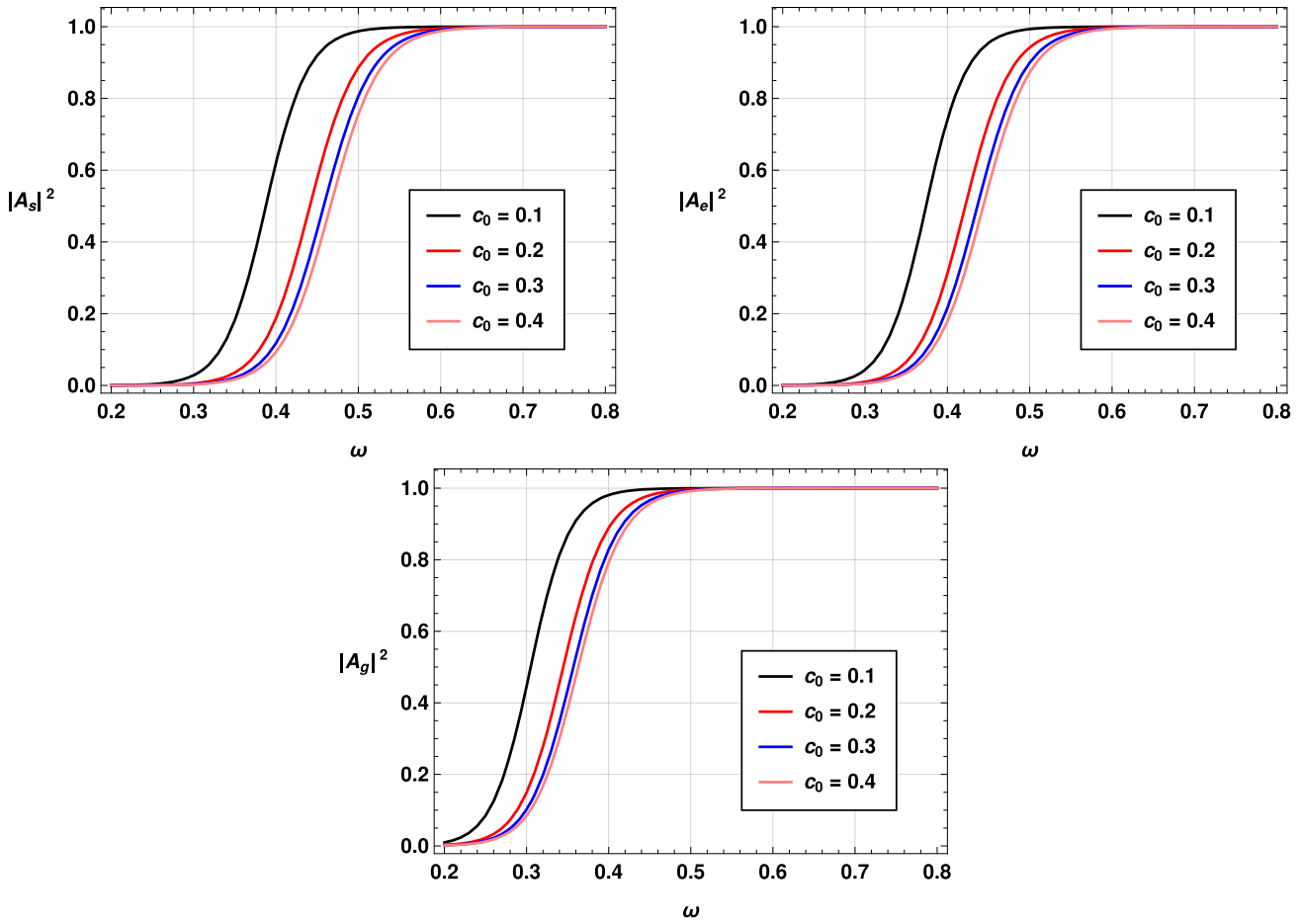

Fig. 23 The greybody factors for massless scalar (first panel), electromagnetic (second panel) and gravitational (third panel) perturbations for different values of the symmergent parameter c_{O} with the parameter values $M = 1$, $G = 1$, $\alpha = 0.9$, $Q = 0.3$ and $l = 2$

model parameter α, greybody bounds decrease significantly. The impacts of parameter l on the greybody bounds are more significant in comparison to the greybody factors discussed in the previous subsection. Again, as the parameter c_{O} increases, the bound on the greybody factor decreases. This observation suggests that CSBHs exhibit stronger barrier properties and possess lower greybody bounds compared to Schwarzschild black holes. The model parameter Q also has a similar impact on the greybody bounds. Overall, the influence of the model parameters for CSBHs on the greybody bounds almost mirrors the effects observed in the case of greybody factors discussed in the previous subsection. Given that greybody factors exhibit similar behavior for both types of perturbations, in this subsection, we have focused solely on scalar perturbations to investigate the greybody bounds.

5 Concluding remarks

In this paper, we have studied charged black hole solutions in the Symmergent gravity [27] by investigating the QNMs and greybody factors of the CSBHs, focusing on scalar, electromagnetic and gravitational perturbations. This work is an extension of our previous work [35]. Here, we have analysed the QNMs and greybody factors in the presence of charge Q. Our analyses reveal that the symmergent parameters α, and the quadratic curvature coupling parameter c_{O} have significant impacts on the QNMs and greybody factors as well as the black hole charge Q and the multipole moment l.

Key insights from our results include:

- Higher multipole moments l lead to stronger potential barriers, higher QNM frequencies, and faster damping rates, with black holes becoming more resistant to perturbations.
- The symmergent parameter α shows a linear increase in both the QNM frequency and damping rate. This suggests that the parameter governs the black hole's ability to trap and damp perturbations, particularly in scalar perturbations.
- The coupling parameter c_{O} also plays a critical role, exhibiting a complex influence on the QNM spectrum

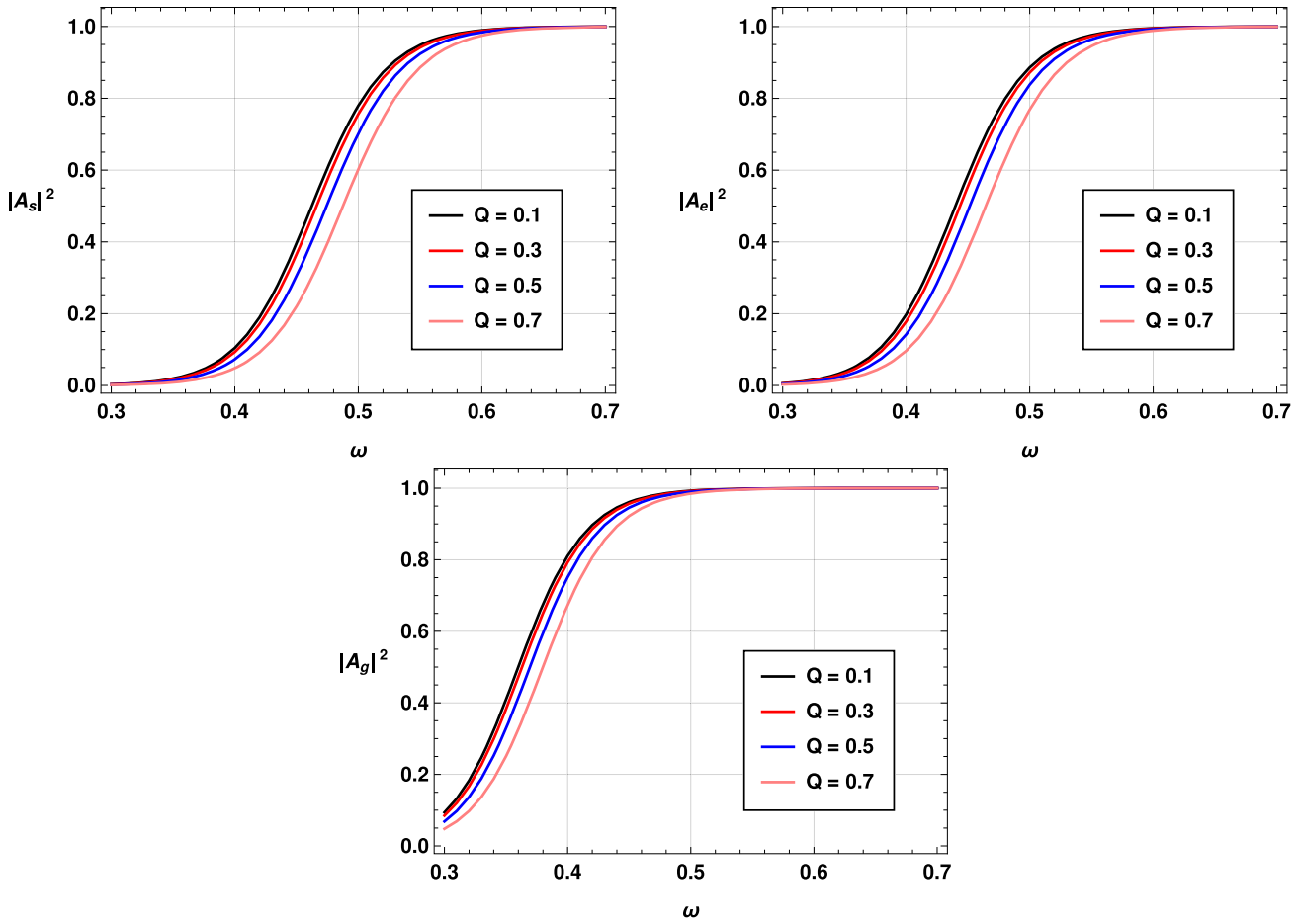

Fig. 24 The greybody factors for massless scalar (first panel), electromagnetic (second panel) and gravitational (third panel) perturbations for different values of the charge parameter Q with the parameter values $M = 1$, $G = 1$, $\alpha = 0.9$, $c_{\mathrm{O}} = 0.4$ and $l = 2$

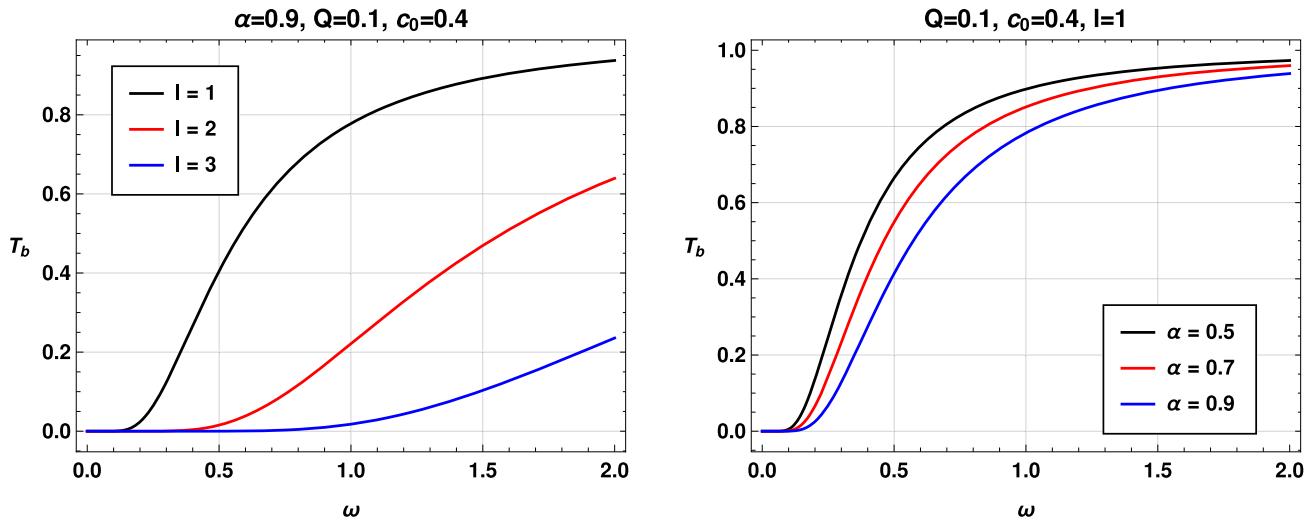

Fig. 25 The greybody bound T_b as a function of the frequency

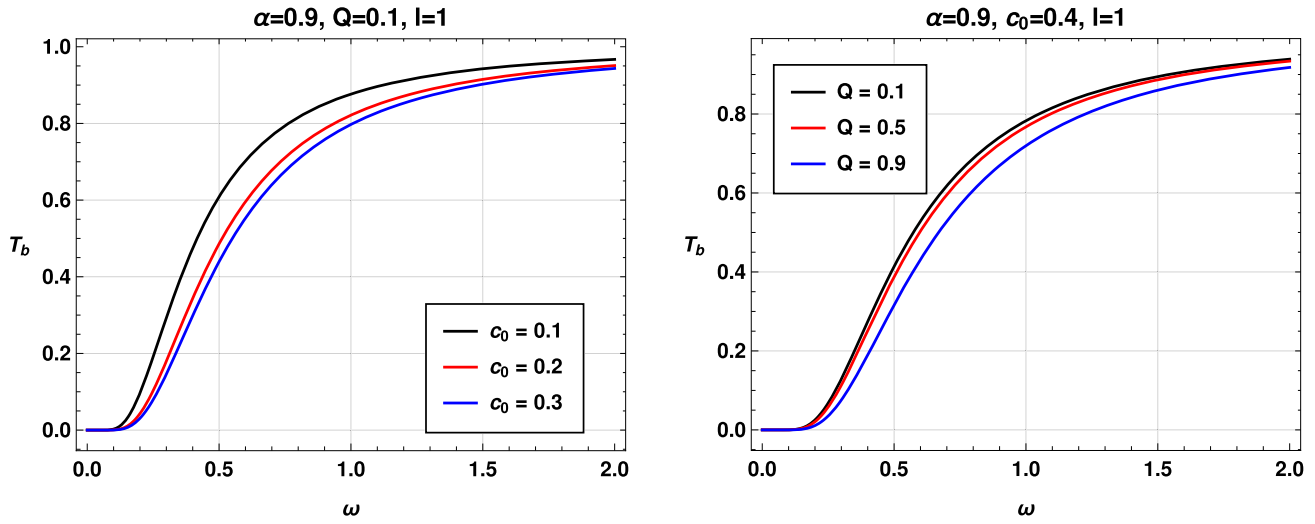

Fig. 26 The greybody bound T_b as a function of the frequency

and the greybody factors. At small values, rapid changes occur in both oscillation frequency and damping rates, but these effects stabilize as c_{O} increases.

- The black hole charge Q increases the potential barrier, resulting in higher frequencies for QNMs, while marginally affecting the damping rate.

The greybody factors of CSBHs were found to differ substantially from those of Schwarzschild black holes. Particularly, the model parameters α and c_{O} play a central role in determining the black hole's absorption and scattering properties. We observed that smaller values of these parameters correspond to higher greybody factors, indicating stronger interactions between the black hole and incoming matter or waves.

Our analysis shows that small positive values of c_{O} result in smaller real QNM frequencies, while small negative values lead to larger frequencies. For asymptotically large positive or negative values of c_{O}, the QNMs approach constant values similar to those in a Schwarzschild black hole. The parameter α has a near-linear effect on both the real and imaginary components of the QNMs, with larger values of α leading to higher frequencies and faster decay rates. Additionally, we observe that the presence of charge Q significantly impacts the QNMs by raising both the frequency and damping rate as Q increases.

Our investigation into scalar, vector and gravitational perturbations shows that scalar perturbations consistently exhibit higher frequencies and shorter lifetimes compared to electromagnetic and gravitational perturbations, a reflection of the stronger interaction between the scalar field and the black hole. The time-domain profiles further highlight that scalar perturbations decay more rapidly, with notable sensitivity to variations in c_{O}, α, and Q.

Regarding the greybody factors, our study indicates that both α and c_{O} have measurable effects on the absorption and scattering behavior of the black hole. We find that smaller values of α increase the greybody factors, suggesting that black holes with reduced α are more effective in absorbing and scattering incoming radiation.

Furthermore, our investigation into the validity of Hod's conjecture offers an additional conceptual perspective on the dynamical stability of these black holes. The conjecture, which relates the damping rate of quasinormal modes to the Hawking temperature, was found to hold robustly across a wide region of the parameter space, thereby reinforcing the consistency of the symmergent black hole solutions with universal stability bounds. However, for very small values of the coupling parameter c_0, we observed notable deviations in which the imaginary part of the frequency can exceed the conjectured limit. This behavior highlights the critical role of c_0 in shaping the black hole's oscillatory properties and suggests a possible observational signature: violations of the conjectured damping bound could manifest as unusually short-lived ringdown signals in gravitational wave data.

Taken together, the combined analysis of QNMs, greybody factors, and the validity of Hod's conjecture not only strengthens the conceptual foundations of our study but also identifies concrete phenomenological features that may be probed in forthcoming observations. The distinct imprints of the parameters α, c_0, and Q on quasinormal spectra and absorption properties provide potential observational targets for future gravitational wave detectors such as LISA and for black hole shadow measurements by the Event Horizon Telescope. With the increasing precision of these facilities, it may soon be possible to place meaningful constraints on symmergent gravity, thereby testing the consistency and viability of the theory. In this sense, our present work establishes a the-

oretical framework that connects the dynamics of charged black holes in symmergent gravity with measurable astrophysical phenomena, offering new opportunities to refine our understanding of black hole physics.

Acknowledgements A. Ö., D. J. G. and B. P. would like to acknowledge networking support by the COST Action CA21106—COSMIC WISPers in the Dark Universe: Theory, astrophysics and experiments (CosmicWISPers). The work of B. P. is supported by Sabancı University, Faculty of Engineering and Natural Sciences. The work of B. P. is supported by the Astrophysics Research Center of the Open University of Israel (ARCO) through The Israeli Ministry of Regional Cooperation. A. Ö. would like to acknowledge networking support of the COST Action CA22113—Fundamental challenges in theoretical physics (THEORY-CHALLENGES), the COST Action CA21136—Addressing observational tensions in cosmology with systematics and fundamental physics (CosmoVerse). A. Ö and B. P. would like to acknowledge networking support by the COST Action CA23130—Bridging high and low energies in search of quantum gravity (BridgeQG), and the COST Action CA23115—Relativistic Quantum Information (RQI) funded by COST (European Cooperation in Science and Technology). A. Ö. and B. P also thank to EMU, TUBITAK, ULAKBIM (Turkiye) and SCOAP3 (Switzerland) for their support.

Data Availability Statement This manuscript has no associated data. [Author's' comment: Data sharing not applicable to this article as no datasets were generated or analysed during the current study.]

Code Availability Statement This manuscript has no associated code/software. [Author's comment: Code/Software sharing not applicable to this article as no code/software was generated or analysed during the current study.]

Funded by SCOAP[3].

References

1. S. Weinberg, Essay: half a century of the Standard Model. Phys. Rev. Lett. **121**(22), 220001 (2018)
2. G. 't Hooft, M.J.G. Veltman, One loop divergencies in the theory of gravitation. Ann. Inst. H. Poincare A Phys. Theor. **20**, 69–94 (1974)
3. J. Oppenheim, A postquantum theory of classical gravity? Phys. Rev. X **13**(4), 041040 (2023)
4. T.D. Galley, F. Giacomini, J.H. Selby, Any consistent coupling between classical gravity and quantum matter is fundamentally irreversible. Quantum **7**, 1142 (2023)
5. S. Weinberg, On the development of effective field theory. Eur. Phys. J. H **46**(1), 6 (2021)
6. E. Gibney, Nature **605**(7911), 604–607 (2022). https://doi.org/10.1038/d41586-022-01388-6
7. J. Polchinski, Renormalization and effective Lagrangians. Nucl. Phys. B **231**, 269–295 (1984)
8. C.P. Burgess, Introduction to effective field theory. Annu. Rev. Nucl. Part. Sci. **57**, 329–362 (2007)
9. M.J.G. Veltman, The infrared–ultraviolet connection. Acta Phys. Polon. B **12**, 437 (1981). (**print-80-0851, MICHIGAN**)
10. H. Umezawa, J. Yukawa, E. Yamada, The problem of vacuum polarization. Prog. Theor. Phys. **3**, 317–318 (1948)
11. G. Kallen, Higher approximations in the external field for the problem of vacuum polarization. Helv. Phys. Acta **22**, 637–654 (1949)
12. F. Englert, R. Brout, Broken symmetry and the mass of gauge vector mesons. Phys. Rev. Lett. **13**, 321–323 (1964)
13. P.W. Higgs, Broken symmetries and the masses of gauge bosons. Phys. Rev. Lett. **13**, 508–509 (1964)
14. G.S. Guralnik, C.R. Hagen, T.W.B. Kibble, Global conservation laws and massless particles. Phys. Rev. Lett. **13**, 585–587 (1964)
15. S. Weinberg, A model of leptons. Phys. Rev. Lett. **19**, 1264–1266 (1967)
16. D. Demir, Gauge and Poincaré properties of the UV cutoff and UV completion in quantum field theory. Phys. Rev. D **107**(10), 105014 (2023)
17. F. Bauer, D.A. Demir, Inflation with non-minimal coupling: metric versus Palatini formulations. Phys. Lett. B **665**, 222–226 (2008)
18. D.A. Demir, Riemann–Eddington theory: incorporating matter, degravitating the cosmological constant. Phys. Rev. D **90**(6), 064017 (2014)
19. V. Vitagliano, T.P. Sotiriou, S. Liberati, The dynamics of metric-affine gravity. Ann. Phys. **326**, 1259-1273 (2011) [Erratum: Annals Phys. **329**, 186-187 (2013)]
20. D. Demir, B. Puliçe, Geometric dark matter. JCAP **04**, 051 (2020)
21. D. Demir, Emergent gravity completion in quantum field theory, and affine condensation in open and closed strings. arXiv:2312.16270 [hep-th]
22. D. Demir, Emergent gravity as the eraser of anomalous gauge boson masses, and QFT-GR concord. Gen. Relativ. Gravit. **53**(2), 22 (2021)
23. D. Demir, Symmergent gravity, seesawic new physics, and their experimental signatures. Adv. High Energy Phys. **2019**, 4652048 (2019)
24. D.A. Demir, Curvature-restored gauge invariance and ultraviolet naturalness. Adv. High Energy Phys. **2016**, 6727805 (2016)
25. D. Demir, Naturally-coupled dark sectors. Galaxies **9**(2), 33 (2021)
26. B. Puliçe, R.C. Pantig, A. Övgün, D. Demir, Asymptotically-flat black hole solutions in symmergent gravity. Fortsch. Phys. **72**, 2300138 (2024). https://doi.org/10.1002/prop.202300138. arXiv:2403.02373 [gr-qc]
27. B. Puliçe, R.C. Pantig, A. Övgün, D. Demir, Constraints on charged symmergent black hole from shadow and lensing. Class. Quantum Gravity **40**(19), 195003 (2023)
28. C.M. Will, The confrontation between general relativity and experiment. Living Rev. Relativ. **17**, 4 (2014). https://doi.org/10.12942/lrr-2014-4. arXiv:1403.7377 [gr-qc]
29. İİ Çimdiker, Starobinsky inflation in emergent gravity. Phys. Dark Univ. **30**, 100736 (2020)
30. İ Çimdiker, D. Demir, A. Övgün, Black hole shadow in symmergent gravity. Phys. Dark Univ. **34**, 100900 (2021)
31. J. Rayimbaev, R.C. Pantig, A. Övgün, A. Abdujabbarov, D. Demir, Quasiperiodic oscillations, weak field lensing and shadow cast around black holes in symmergent gravity. Ann. Phys. **454**, 169335 (2023)
32. R.C. Pantig, A. Övgün, D. Demir, Testing symmergent gravity through the shadow image and weak field photon deflection by a

rotating black hole using the M87* and Sgr. A* results. Eur. Phys. J. C **83**, 250 (2023)
33. R. Ali, R. Babar, Z. Akhtar, A. Övgün, Thermodynamics and logarithmic corrections of symmergent black holes. Results Phys. **46**, 106300 (2023)
34. İİ Çimdiker, A. Övgün, D. Demir, Thin accretion disk images of the black hole in symmergent gravity. Class. Quantum Gravity **40**(18), 184001 (2023)
35. D.J. Gogoi, A. Övgün, D. Demir, Phys. Dark Univ. **42**, 101314 (2023). https://doi.org/10.1016/j.dark.2023.101314. arXiv:2306.09231 [gr-qc]
36. B.P. Abbott et al. [LIGO Scientific and Virgo], Observation of gravitational waves from a binary black hole merger. Phys. Rev. Lett. **116**(6), 061102 (2016) https://doi.org/10.1103/PhysRevLett.116.061102. arXiv:1602.03837 [gr-qc]
37. R. Abbott et al. [LIGO Scientific, KAGRA and VIRGO], Observation of gravitational waves from two neutron star–black hole coalescences. Astrophys. J. Lett. **915**(1), L5 (2021). https://doi.org/10.3847/2041-8213/ac082e. arXiv:2106.15163 [astro-ph.HE]
38. K. Akiyama et al. [Event Horizon Telescope], First Sagittarius A* Event Horizon Telescope Results. I. The shadow of the supermassive black hole in the Center of the Milky Way. Astrophys. J. Lett. **930**(2), L12 (2022). https://doi.org/10.3847/2041-8213/ac6674. arXiv:2311.08680 [astro-ph.HE]
39. A.D. Goulding, J.E. Greene, D.J. Setton, I. Labbe, R. Bezanson, T.B. Miller, H. Atek, A. Bogdan, G. Brammer, I. Chemerynska et al., UNCOVER: the growth of the first massive black holes from JWST/NIRSpec—spectroscopic redshift confirmation of an X-ray luminous AGN at z = 10.1. Astrophys. J. Lett. **955**(1), L24 (2023). https://doi.org/10.3847/2041-8213/acf7c5. arXiv:2308.02750 [astro-ph.GA]
40. S. Aneesh, S. Bose, S. Kar, Gravitational waves from quasinormal modes of a class of Lorentzian wormholes. Phys. Rev. D **97**(12), 124004 (2018)
41. D.M. Eardley, D.L. Lee, A.P. Lightman, R.V. Wagoner, C.M. Will, Gravitational-wave observations as a tool for testing relativistic gravity. Phys. Rev. Lett. **30**, 884–886 (1973). https://doi.org/10.1103/PhysRevLett.30.884
42. T. Regge, J.A. Wheeler, Stability of a Schwarzschild singularity. Phys. Rev. **108**, 1063–1069 (1957)
43. C.V. Vishveshwara, Stability of the Schwarzschild metric. Phys. Rev. D **1**, 2870–2879 (1970)
44. F.J. Zerilli, Effective potential for even parity Regge–Wheeler gravitational perturbation equations. Phys. Rev. Lett. **24**, 737–738 (1970)
45. F.J. Zerilli, Gravitational field of a particle falling in a Schwarzschild geometry analyzed in tensor harmonics. Phys. Rev. D **2**, 2141–2160 (1970)
46. F.J. Zerilli, Perturbation analysis for gravitational and electromagnetic radiation in a Reissner–Nordstroem geometry. Phys. Rev. D **9**, 860–868 (1974)
47. V. Moncrief, Gauge-invariant perturbations of Reissner–Nordstrom black holes. Phys. Rev. D **12**, 1526–1537 (1975)
48. S.A. Teukolsky, Rotating black holes—separable wave equations for gravitational and electromagnetic perturbations. Phys. Rev. Lett. **29**, 1114–1118 (1972)
49. S. Chandrasekhar, S. Detweiler, The quasi-normal modes of the Schwarzschild black hole. Proc. R. Soc. Lond. A **344**, 441 (1975)
50. S. Chandrasekhar, *The Mathematical Theory of Black Holes* (Clarendon, Oxford, 1985)
51. R.A. Konoplya, A. Zhidenko, Quasinormal modes of black holes: from astrophysics to string theory. Rev. Mod. Phys. **83**, 793–836 (2011)
52. E. Berti, V. Cardoso, A.O. Starinets, Quasinormal modes of black holes and black branes. Class. Quantum Gravity **26**, 163001 (2009)
53. R.G. Daghigh, M.D. Green, Highly real, highly damped, and other asymptotic quasinormal modes of Schwarzschild–anti De Sitter black holes. Class. Quantum Gravity **26**, 125017 (2009)
54. R.G. Daghigh, M.D. Green, J.C. Morey, Significance of black hole quasinormal modes: a closer look. Phys. Rev. D **101**(10), 104009 (2020)
55. R.G. Daghigh, M.D. Green, J.C. Morey, G. Kunstatter, Scalar perturbations of a single-horizon regular black hole. Phys. Rev. D **102**(10), 104040 (2020)
56. R.G. Daghigh, G. Kunstatter, J. Ziprick, The mystery of the asymptotic quasinormal modes of Gauss–Bonnet black holes. Class. Quantum Gravity **24**, 1981–1992 (2007)
57. R.G. Daghigh, M.D. Green, J.C. Morey, Calculating quasinormal modes of Schwarzschild anti-de Sitter black holes using the continued fraction method. Phys. Rev. D **107**(2), 024023 (2023)
58. E. Berti, V. Cardoso, C.M. Will, On gravitational-wave spectroscopy of massive black holes with the space interferometer LISA. Phys. Rev. D **73**, 064030 (2006)
59. V. Ferrari, L. Gualtieri, Quasi-normal modes and gravitational wave astronomy. Gen. Relativ. Gravit. **40**, 945–970 (2008)
60. M. Chabab, H. El Moumni, S. Iraoui, K. Masmar, Behavior of quasinormal modes and high dimension RN–AdS black hole phase transition. Eur. Phys. J. C **76**(12), 676 (2016)
61. M. Chabab, H. El Moumni, S. Iraoui, K. Masmar, Phase transition of charged-AdS black holes and quasinormal modes: a time domain analysis. Astrophys. Space Sci. **362**(10), 192 (2017)
62. S. Lepe, J. Saavedra, Quasinormal modes, superradiance and area spectrum for 2 + 1 acoustic black holes. Phys. Lett. B **617**, 174–181 (2005)
63. P.A. González, E. Papantonopoulos, J. Saavedra, Y. Vásquez, Superradiant instability of near extremal and extremal four-dimensional charged hairy black hole in anti-de Sitter spacetime. Phys. Rev. D **95**(6), 064046 (2017)
64. S. Fernando, Quasinormal modes of dilaton-de Sitter black holes: scalar perturbations. Gen. Relativ. Gravit. **48**(3), 24 (2016)
65. S. Fernando, Quasi-normal modes and the area spectrum of a near extremal de Sitter black hole with conformally coupled scalar field. Mod. Phys. Lett. A **30**(11), 1550057 (2015)
66. S. Fernando, J. Correa, Quasinormal modes of Bardeen black hole: scalar perturbations. Phys. Rev. D **86**, 064039 (2012)
67. S. Fernando, Quasinormal modes of charged scalars around dilaton black holes in 2 + 1 dimensions: exact frequencies. Phys. Rev. D **77**, 124005 (2008)
68. M. Khodadi, K. Nozari, H. Abedi, S. Capozziello, Planck scale effects on the stochastic gravitational wave background generated from cosmological hadronization transition: a qualitative study. Phys. Lett. B **783**, 326–333 (2018)
69. D.J. Gogoi, U.D. Goswami, Quasinormal modes and Hawking radiation sparsity of GUP corrected black holes in bumblebee gravity with topological defects. JCAP **06**(06), 029 (2022)
70. D.J. Gogoi, A. Övgün, M. Koussour, Quasinormal modes of black holes in f(Q) gravity. Eur. Phys. J. C **83**(8), 700 (2023)
71. D.J. Gogoi, R. Karmakar, U.D. Goswami, Quasinormal modes of nonlinearly charged black holes surrounded by a cloud of strings in Rastall gravity. Int. J. Geom. Methods Mod. Phys. **20**(01), 2350007 (2023)
72. D.J. Gogoi, U.D. Goswami, Quasinormal modes of black holes with non-linear-electrodynamic sources in Rastall gravity. Phys. Dark Univ. **33**, 100860 (2021)
73. R. Oliveira, D.M. Dantas, C.A.S. Almeida, Quasinormal frequencies for a black hole in a bumblebee gravity. EPL **135**(1), 10003 (2021)
74. X.M. Kuang, J.P. Wu, Thermal transport and quasi-normal modes in Gauss–Bonnet-axions theory. Phys. Lett. B **770**, 117–123 (2017)

75. M. Kac, Can one hear the shape of a drum? Am. Math. Mon. **73**, 1–23 (1966). https://doi.org/10.2307/2313748
76. N. Andersson, S. Linnæus, Quasinormal modes of a Schwarzschild black hole: improved phase-integral treatment. Phys. Rev. D **46**(10), 4179 (1992)
77. N. Andersson, Complex angular momenta and the black hole glory. Class. Quantum Gravity **11**, 3003–3012 (1994)
78. N. Andersson, Scattering of massless scalar waves by a Schwarzschild black hole: a phase integral study. Phys. Rev. D **52**, 1808–1820 (1995)
79. N. Andersson, H. Onozawa, Quasinormal modes of nearly extreme Reissner–Nordstrom black holes. Phys. Rev. D **54**, 7470–7475 (1996)
80. E. Maggio, A. Testa, S. Bhagwat, P. Pani, Analytical model for gravitational-wave echoes from spinning remnants. Phys. Rev. D **100**(6), 064056 (2019)
81. R.A. Konoplya, A. Zhidenko, Can the abyss swallow gravitational waves or why we do not observe echoes? EPL **138**, 49001 (2022)
82. R.A. Konoplya, Z. Stuchlík, A. Zhidenko, Echoes of compact objects: new physics near the surface and matter at a distance. Phys. Rev. D **99**(2), 024007 (2019)
83. V. Cardoso, E. Franzin, P. Pani, Is the gravitational-wave ringdown a probe of the event horizon?, Phys. Rev. Lett. **116**(17), 171101 (2016) [Erratum: Phys. Rev. Lett. **117**, no.8, 089902 (2016)]
84. V. Cardoso, S. Hopper, C.F.B. Macedo, C. Palenzuela, P. Pani, Gravitational-wave signatures of exotic compact objects and of quantum corrections at the horizon scale. Phys. Rev. D **94**(8), 084031 (2016)
85. L. Visinelli, N. Bolis, S. Vagnozzi, Brane-world extra dimensions in light of GW170817. Phys. Rev. D **97**(6), 064039 (2018)
86. S. Vagnozzi, Implications of the NANOGrav results for inflation. Mon. Not. R. Astron. Soc. **502**(1), L11–L15 (2021)
87. A. Casalino, M. Rinaldi, L. Sebastiani, S. Vagnozzi, Alive and well: mimetic gravity and a higher-order extension in light of GW170817. Class. Quantum Gravity **36**(1), 017001 (2019)
88. A. Casalino, M. Rinaldi, L. Sebastiani, S. Vagnozzi, Mimicking dark matter and dark energy in a mimetic model compatible with GW170817. Phys. Dark Univ. **22**, 108 (2018)
89. V. Cardoso, P. Pani, Tests for the existence of black holes through gravitational wave echoes. Nat. Astron. **1**(9), 586–591 (2017)
90. S. Vagnozzi, Inflationary interpretation of the stochastic gravitational wave background signal detected by pulsar timing array experiments. JHEAp **39**, 81–98 (2023)
91. M. Benetti, L.L. Graef, S. Vagnozzi, Primordial gravitational waves from NANOGrav: a broken power-law approach. Phys. Rev. D **105**(4), 043520 (2022)
92. W. Yang, S. Vagnozzi, E. Di Valentino, R.C. Nunes, S. Pan, D.F. Mota, Listening to the sound of dark sector interactions with gravitational wave standard sirens. JCAP **07**, 037 (2019)
93. R.C. Pantig, L. Mastrototaro, G. Lambiase, A. Övgün, Shadow, lensing, quasinormal modes, greybody bounds and neutrino propagation by dyonic ModMax black holes. Eur. Phys. J. C **82**(12), 1155 (2022)
94. G. Lambiase, R.C. Pantig, D.J. Gogoi, A. Övgün, Investigating the connection between generalized uncertainty principle and asymptotically safe gravity in black hole signatures through shadow and quasinormal modes. Eur. Phys. J. C **83**(7), 679 (2023)
95. Y. Yang, D. Liu, A. Övgün, Z.W. Long, Z. Xu, Probing hairy black holes caused by gravitational decoupling using quasinormal modes and greybody bounds. Phys. Rev. D **107**(6), 064042 (2023)
96. M. Okyay, A. Övgün, Nonlinear electrodynamics effects on the black hole shadow, deflection angle, quasinormal modes and greybody factors. JCAP **01**(01), 009 (2022)
97. R.G. Daghigh, M.D. Green, Validity of the WKB approximation in calculating the asymptotic quasinormal modes of black holes. Phys. Rev. D **85**, 127501 (2012)
98. A. Zhidenko, Quasinormal modes of Schwarzschild de Sitter black holes. Class. Quantum Gravity **21**, 273–280 (2004)
99. A. Zhidenko, Quasi-normal modes of the scalar hairy black hole. Class. Quantum Gravity **23**, 3155–3164 (2006)
100. A. Al-Badawi, Y. Sekhmani, K. Boshkayev, Shadow, quasinormal modes and Hawking radiation of ModMax black holes in a quintessence background. Phys. Dark Univ. **48**, 101865 (2025). https://doi.org/10.1016/j.dark.2025.101865
101. Y. Sekhmani, D.J. Gogoi, S.K. Maurya, K. Boshkayev, M.K. Jasim, Quasinormal modes and greybody bounds of black holes endowed with modified Chaplygin gas. JHEAp **45**, 200–213 (2025). https://doi.org/10.1016/j.jheap.2024.11.020
102. Y. Sekhmani, D.J. Gogoi, Electromagnetic quasinormal modes of dyonic AdS black holes with quasitopological electromagnetism in a Horndeski gravity theory mimicking EGB gravity at D → 4. Int. J. Geom. Methods Mod. Phys. **20**(09), 2350160 (2023). https://doi.org/10.1142/S0219887823501608. arXiv:2306.02919 [gr-qc]
103. A.N. Malybayev, K.A. Boshkayev, V.D. Ivashchuk, Quasinormal modes in the field of a dyon-like dilatonic black hole. Eur. Phys. J. C **81**(5), 475 (2021). https://doi.org/10.1140/epjc/s10052-021-09252-z. arXiv:2103.10920 [gr-qc]
104. Z. Hu, D.D. Doneva, Z. Wang, V. Paschalidis, G. Bozzola, S.S. Yazadjiev, L. Shao, Ringdown mode amplitudes of charged binary black holes. arXiv:2509.07111 [gr-qc]
105. R.F. Rosato, P. Pani, Universality of late-time ringdown tails. Phys. Rev. D **112**(2), 024080 (2025). https://doi.org/10.1103/4yvq-57x6. arXiv:2505.08877 [gr-qc]
106. M.A.M. Smith, V. Paschalidis, G. Bozzola, High-energy interactions of charged black holes in full general relativity. I. Zoom-whirl orbits and universality with the irreducible mass. Phys. Rev. D **111**(10), 104031 (2025). https://doi.org/10.1103/PhysRevD.111.104031. arXiv:2411.11960 [gr-qc]
107. A. De Felice, S. Tsujikawa, Can we distinguish black holes with electric and magnetic charges from quasinormal modes? Phys. Rev. D **109**(8), 084022 (2024). https://doi.org/10.1103/PhysRevD.109.084022. arXiv:2312.03191 [gr-qc]
108. H.T. Wang, P.C. Li, J.L. Jiang, G.W. Yuan, Y.M. Hu, Y.Z. Fan, Constrains on the electric charges of the binary black holes with GWTC-1 events. Eur. Phys. J. C **81**(8), 769 (2021). https://doi.org/10.1140/epjc/s10052-021-09555-1. arXiv:2004.12421 [gr-qc]
109. S.R. Dolan, M.A.A. de Paula, L.C.S. Leite, L.C.B. Crispino, Superradiant instability of a charged regular black hole. Phys. Rev. D **109**(12), 124037 (2024). https://doi.org/10.1103/PhysRevD.109.124037. arXiv:2401.14967 [gr-qc]
110. G. Carullo, D. Laghi, N.K. Johnson-McDaniel, W. Del Pozzo, O.J.C. Dias, M. Godazgar, J.E. Santos, Constraints on Kerr–Newman black holes from merger-ringdown gravitational-wave observations. Phys. Rev. D **105**(6), 062009 (2022). https://doi.org/10.1103/PhysRevD.105.062009. arXiv:2109.13961 [gr-qc]
111. G. Bozzola, V. Paschalidis, General relativistic simulations of the quasicircular inspiral and merger of charged black holes: GW150914 and fundamental physics implications. Phys. Rev. Lett. **126**(4), 041103 (2021). https://doi.org/10.1103/PhysRevLett.126.041103. arXiv:2006.15764 [gr-qc]
112. S.L. Liebling, C. Palenzuela, Electromagnetic luminosity of the coalescence of charged black hole binaries. Phys. Rev. D **94**(6), 064046 (2016). https://doi.org/10.1103/PhysRevD.94.064046. arXiv:1607.02140 [gr-qc]
113. E. Berti, K.D. Kokkotas, Quasinormal modes of Kerr–Newman black holes: coupling of electromagnetic and gravitational perturbations. Phys. Rev. D **71**, 124008 (2005). https://doi.org/10.1103/PhysRevD.71.124008. arXiv:gr-qc/0502065 [gr-qc]
114. J.L. Blázquez-Salcedo, F.S. Khoo, Quasinormal modes of slowly rotating Kerr–Newman black holes using the double series

method. Phys. Rev. D **107**(8), 084031 (2023). https://doi.org/10.1103/PhysRevD.107.084031. arXiv:2212.00054 [gr-qc]
115. P.A. González, E. Papantonopoulos, Á. Rincón, Y. Vásquez, Quasinormal modes of massive scalar fields in four-dimensional wormholes: anomalous decay rate. Phys. Rev. D **106**(2), 024050 (2022)
116. Á. Rincón, G. Panotopoulos, Greybody factors and quasinormal modes for a nonminimally coupled scalar field in a cloud of strings in (2+1)-dimensional background. Eur. Phys. J. C **78**(10), 858 (2018)
117. G.W. Gibbons, K.I. Maeda, Black holes and membranes in higher dimensional theories with dilaton fields. Nucl. Phys. B **298**, 741–775 (1988). https://doi.org/10.1016/0550-3213(88)90006-5
118. D. Garfinkle, G.T. Horowitz, A. Strominger, Charged black holes in string theory. Phys. Rev. D **43**, 3140 (1991) [Erratum: Phys. Rev. D **45**, 3888 (1992)] https://doi.org/10.1103/PhysRevD.43.3140
119. M. Demianski, Static electromagnetic geon. Found. Phys. **16**, 187–190 (1986). https://doi.org/10.1007/BF01889380
120. T.K. Dey, Born–Infeld black holes in the presence of a cosmological constant. Phys. Lett. B **595**, 484–490 (2004). https://doi.org/10.1016/j.physletb.2004.06.047. arXiv:hep-th/0406169
121. R.G. Cai, D.W. Pang, A. Wang, Born–Infeld black holes in (A)dS spaces. Phys. Rev. D **70**, 124034 (2004). https://doi.org/10.1103/PhysRevD.70.124034. arXiv:hep-th/0410158
122. P. Bizon, Colored black holes. Phys. Rev. Lett. **64**, 2844–2847 (1990). https://doi.org/10.1103/PhysRevLett.64.2844
123. N. Straumann, Z.H. Zhou, Instability of the Bartnik–Mckinnon solution of the Einstein Yang–Mills equations. Phys. Lett. B **237**, 353–356 (1990). https://doi.org/10.1016/0370-2693(90)91188-H
124. R. Emparan, H.S. Reall, A rotating black ring solution in five-dimensions. Phys. Rev. Lett. **88**, 101101 (2002). https://doi.org/10.1103/PhysRevLett.88.101101. arXiv:hep-th/0110260
125. H. Elvang, R. Emparan, D. Mateos, H.S. Reall, A supersymmetric black ring. Phys. Rev. Lett. **93**, 211302 (2004). https://doi.org/10.1103/PhysRevLett.93.211302. arXiv:hep-th/0407065
126. B.P. Abbott et al. [LIGO Scientific and Virgo], Observation of gravitational waves from a binary black hole merger. Phys. Rev. Lett. **116**(6), 061102 (2016)
127. B.P. Abbott et al. [LIGO Scientific and Virgo], GW151226: observation of gravitational waves from a 22-solar-mass binary black hole coalescence. Phys. Rev. Lett. **116**(24), 241103 (2016)
128. A. Övgün, K. Jusufi, Quasinormal modes and greybody factors of $f(R)$ gravity minimally coupled to a cloud of strings in $2+1$ dimensions. Ann. Phys. **395**, 138–151 (2018)
129. D.J. Gogoi, U.D. Goswami, Tideless traversable wormholes surrounded by cloud of strings in f(R) gravity. JCAP **02**, 027 (2023)
130. S. Hod, Universal bound on dynamical relaxation times and black-hole quasinormal ringing. Phys. Rev. D **75**, 064013 (2007). https://doi.org/10.1103/PhysRevD.75.064013. arXiv:gr-qc/0611004
131. E. Berti, V. Cardoso, K.D. Kokkotas, H. Onozawa, Highly damped quasinormal modes of Kerr black holes. Phys. Rev. D **68**, 124018 (2003). https://doi.org/10.1103/PhysRevD.68.124018. arXiv:hep-th/0307013
132. A. Ghosh, S. Shankaranarayanan, S. Das, High frequency quasinormal modes for black holes with generic singularities. II. Asymptotically non-flat spacetimes. Class. Quantum Gravity **23**, 1851–1874 (2006). https://doi.org/10.1088/0264-9381/23/6/003. arXiv:hep-th/0510186
133. M.S. Churilova, Z. Stuchlik, Quasinormal modes of black holes in 5D Gauss–Bonnet gravity combined with non-linear electrodynamics. Ann. Phys. **418**, 168181 (2020). https://doi.org/10.1016/j.aop.2020.168181. arXiv:1910.12660 [gr-qc]
134. M.A. Cuyubamba, R.A. Konoplya, A. Zhidenko, Quasinormal modes and a new instability of Einstein–Gauss–Bonnet black holes in the de Sitter world. Phys. Rev. D **93**(10), 104053 (2016). https://doi.org/10.1103/PhysRevD.93.104053. arXiv:1604.03604 [gr-qc]
135. R.A. Konoplya, A. Zhidenko, How general is the strong cosmic censorship bound for quasinormal modes? JCAP **11**, 028 (2022). https://doi.org/10.1088/1475-7516/2022/11/028. arXiv:2210.04314 [gr-qc]
136. A.F. Zinhailo, Quasinormal modes of Dirac field in the Einstein-Dilaton-Gauss–Bonnet and Einstein–Weyl gravities. Eur. Phys. J. C **79**(11), 912 (2019). https://doi.org/10.1140/epjc/s10052-019-7425-9. arXiv:1909.12664 [gr-qc]
137. S.W. Hawking, Particle creation by black holes. Commun. Math. Phys. **43**, 199-220 (1975) [Erratum: Commun. Math. Phys. **46**, 206 (1976)]
138. D. Singleton, S. Wilburn, Hawking radiation, Unruh radiation and the equivalence principle. Phys. Rev. Lett. **107**, 081102 (2011)
139. V. Akhmedova, T. Pilling, A. de Gill, D. Singleton, Temporal contribution to gravitational WKB-like calculations. Phys. Lett. B **666**, 269–271 (2008)
140. J.M. Maldacena, A. Strominger, Black hole grey body factors and d-brane spectroscopy. Phys. Rev. D **55**, 861–870 (1997)
141. S. Fernando, Greybody factors of charged dilaton black holes in 2 + 1 dimensions. Gen. Relativ. Gravit. **37**, 461–481 (2005)
142. Y. Yang, D. Liu, A. Övgün, Z.W. Long, Z. Xu, Quasinormal modes of Kerr-like black bounce spacetime. arXiv:2205.07530 [gr-qc]
143. G. Panotopoulos, A. Rincón, Greybody factors for a minimally coupled scalar field in three-dimensional Einstein-power-Maxwell black hole background. Phys. Rev. D **97**(8), 085014 (2018)
144. G. Panotopoulos, Á. Rincón, Greybody factors for a nonminimally coupled scalar field in BTZ black hole background. Phys. Lett. B **772**, 523–528 (2017)
145. J. Ahmed, K. Saifullah, Greybody factor of a scalar field from Reissner–Nordström–de Sitter black hole. Eur. Phys. J. C **78**(4), 316 (2018)
146. W. Javed, M. Aqib, A. Övgün, Effect of the magnetic charge on weak deflection angle and greybody bound of the black hole in Einstein–Gauss–Bonnet gravity. Phys. Lett. B **829**, 137114 (2022)
147. A. Al-Badawi, S. Kanzi, İ Sakallı, Fermionic and bosonic greybody factors as well as quasinormal modes for charged Taub NUT black holes. Ann. Phys. **452**, 169294 (2023)
148. C.Y. Chen, P. Chen, Gravitational perturbations of nonsingular black holes in conformal gravity. Phys. Rev. D **99**(10), 104003 (2019)
149. M. Bouhmadi-López, S. Brahma, C.-Y. Chen, P. Chen, D. Yeom, A consistent model of non-singular Schwarzschild black hole in loop quantum gravity and its quasinormal modes. J. Cosmol. Astropart. Phys. **07**, 066 (2020)
150. R. Bécar, P.A. González, E. Papantonopoulos, Y. Vásquez, Massive scalar field perturbations of 4D de Sitter–Einstein–Gauss–Bonnet black holes. Phys. Rev. D **111**(12), 124013 (2025)
151. A. Sommerfeld, *Partial Differential Equations in Physics* (Academic Press, New York, 1949)
152. H.T. Cho, A.S. Cornell, J. Doukas, W. Naylor, Black hole quasinormal modes using the asymptotic iteration method. Class. Quantum Gravity **27**, 155004 (2010)
153. H.T. Cho, A.S. Cornell, J. Doukas, W. Naylor, Asymptotic iteration method for spheroidal harmonics of higher-dimensional Kerr–(A)DS black holes. Phys. Rev. D **80**, 064022 (2009)
154. S. Ponglertsakul, T. Tangphati, P. Burikham, Near-horizon quasinormal modes of charged scalar around a general spherically symmetric black hole. Phys. Rev. D **99**, 084002 (2019)
155. S. Ponglertsakul, B. Gwak, Massive scalar perturbations on Myers–Perry–de Sitter black holes with a single rotation. Eur. Phys. J. C **80**, 1023 (2020)

156. B.F. Schutz, C.M. Will, Black hole normal modes—a semi analytic approach. Astrophys. J. **291**, L33 (1985)
157. S. Iyer, C.M. Will, Black-hole normal modes: a WKB approach. I. Foundations and application of a higher-order WKB analysis of potential-barrier scattering. Phys. Rev. D **35**, 3621 (1987)
158. R.A. Konoplya, Quasinormal behavior of the D-dimensional Schwarzschild black hole and the higher order WKB approach. Phys. Rev. D **68**, 024018 (2003)
159. J. Matyjasek, M. Telecka, Quasinormal modes of black holes. II. Padé Summation of the higher-order WKB terms. Phys. Rev. D **100**, 124006 (2019)
160. C. Gundlach, R.H. Price, J. Pullin, Late time behavior of stellar collapse and explosions: 2. Nonlinear evolution. Phys. Rev. D **49**, 890 (1994)
161. R.A. Konoplya, A. Zhidenko, A.F. Zinhailo, Higher order WKB formula for quasinormal modes and grey-body factors: recipes for quick and accurate calculations. Class. Quantum Gravity **36**, 155002 (2019)
162. M. Visser, Some general bounds for 1-D scattering. Phys. Rev. A **59**, 427–438 (1999)
163. P. Boonserm, M. Visser, Bounding the greybody factors for Schwarzschild black holes. Phys. Rev. D **78**, 101502 (2008)
164. P. Boonserm, T. Ngampitipan, P. Wongjun, Greybody factor for black holes in dRGT massive gravity. Eur. Phys. J. C **78**(6), 492 (2018)
165. F. Gray, M. Visser, Greybody factors for Schwarzschild black holes: path-ordered exponentials and product integrals. Universe **4**(9), 93 (2018)
166. T. Ngampitipan, P. Boonserm, Bounding the greybody factors for non-rotating black holes. Int. J. Mod. Phys. D **22**, 1350058 (2013)
167. A. Chowdhury, N. Banerjee, Greybody factor and sparsity of Hawking radiation from a charged spherical black hole with scalar hair. Phys. Lett. B **805**, 135417 (2020)
168. Y.G. Miao, Z.M. Xu, Hawking radiation of five-dimensional charged black holes with scalar fields. Phys. Lett. B **772**, 542–546 (2017)
169. S.W. Hawking, Black hole explosions. Nature **248**, 30–31 (1974)
170. Y. Liu, Hawking temperature and the bound on greybody factors in $D = 4$ double field theory. Eur. Phys. J. C **82**(11), 1054 (2022)
171. S. Barman, The Hawking effect and the bounds on greybody factor for higher dimensional Schwarzschild black holes. Eur. Phys. J. C **80**(1), 50 (2020)
172. P. Boonserm, T. Ngampitipan, P. Wongjun, Greybody factor for black string in dRGT massive gravity. Eur. Phys. J. C **79**(4), 330 (2019)
173. V. Ferrari, L. Gualtieri, Quasi-normal modes and gravitational wave astronomy. Gen. Relativ. Gravit. **40**, 945 (2008)
174. G. Panotopoulos, F. Tello-Ortiz, Quantum black holes: perihelion advance, quasi normal modes and classical/topological thermodynamics. Phys. Lett. B **868**, 139769 (2025)